PAPER • OPEN ACCESS

Automated calibration of model-driven reconstructions in atom probe tomography

View the article online for updates and enhancements.

Automated calibration of model-driven reconstructions in atom probe tomography

Charles Fletcher[1] , **Michael P Moody**[1,*] , **Claudia Fleischmann**[2,3] , **Masoud Dialameh**[2], **Clement Porret**[2] , **Brian Geiser**[4] **and Daniel Haley**[1]

[1] Department of Materials, University of Oxford, Parks Road, Oxford OX1 3PH, United Kingdom
[2] imec, Kapeldreef 75, 3001 Heverlee, Belgium
[3] Quantum Solid State Physics, KU Leuven, Celestijnenlaan 200D, 3001 Leuven, Belgium
[4] Cameca Instruments Inc., 5470 Nobel Drive, Madison, WI 53711, United States of America

E-mail: michael.moody@materials.ox.ac.uk

Abstract

Traditional reconstruction protocols in atom probe tomography frequently feature image distortions for multiphase materials, due to inaccurate geometric assumptions regarding specimen evolution. In this work, the authors' outline a new reconstruction protocol capable of correcting for many of these distortions. This new method uses predictions from a previously developed physical model for specimen field evaporation. The application of this new model-driven approach to both an experimental semiconductor multilayer system and a fin field-effect transistor device (finFET) is considered. In both systems, a significant reduction in multiphase image distortions when using this new algorithm is clearly demonstrated. By being able to quantitatively compare model predictions with experiment, such a method could also be applied to testing and validating new developments in field evaporation theory.

Supplementary material for this article is available online

Keywords: atom probe tomography, semiconductor imaging, level set method, field evaporation, data reconstruction, optimisation, correlative microscopy

(Some figures may appear in colour only in the online journal)

1. Introduction

Atom probe tomography (APT) is a materials characterisation technique that aims to form a 3D image at a near atomic resolution within a material subvolume. By combining analysis data from a two-dimensional position-sensitive detector with a mass spectrometer, individual ion types and original positions can be estimated via an algorithmic process known as reconstruction. These algorithms assume a simple model for specimen evolution during APT analysis. The most common reconstruction protocols are mathematical projection-based models [1–5]. These projection-based models assume a specimen apex that remains hemispherical throughout APT analyses, and that the charged optics of evaporated ions' are well described by some mathematical projection between the hemispherical apex and planar detector. These protocols' have the advantage of simple geometric assumptions, requiring limited prior information, whilst performing well for a wide variety of material systems. However, for multiphase

specimens, the apex shape and trajectory assumptions made by projection-based models frequently break down, introducing phase-specific distortions into their reconstructions. Physically correcting these distortions will require improved models for multiphase specimen evaporation that are sufficiently 'quick' to drive a reconstruction protocol.

In our previous works [6, 7], a simulation framework was developed allowing for rapid simulation of specimen evaporation in three-dimensions (3D). Whilst this new model lacks the accuracy of the current state-of-the-art atomic-scale models [8–10], its underlying continuum assumption enables practical simulation times, making it feasible to reconstruct experimental APT analyses using this continuum model. This reconstruction capability was demonstrated through a proof-of-concept model-driven reconstruction algorithm, which when applied to a fin field-effect transistor (FinFET) successfully corrected for phase-specific distortions within the structure's central fin [7].

Whilst this reconstruction scheme can correct for multiphase distortions introduced by projection-based protocols, the approach has the downside of requiring a higher degree of prior information in order to define the more physically accurate and detailed evaporation model. This includes knowledge of the initial specimen surface and internal phase geometries, the governing physical evaporation laws, and any material-specific evaporation parameters. Assuming that the model's initial specimen surface and phase geometries can be sufficiently constrained through electron microscopy [7, 11, 12], this still leaves a potentially large number of free model parameters that must be tuned. These parameters include the alignment of the simulated specimen with respect to the detector, as well as the parameters governing the evaporation mechanics of particular model phases.

This work sets out a new approach for constraining these alignment and phase-specific evaporation parameters directly from the experimental APT data, automatically optimising the final image quality of the model-driven reconstruction. In addition, a method is also proposed for partially relaxing the constraints imposed by the assumed model's charged optics through a parameterised transformation known as a diffeomorphism. By determining a diffeomorphism that reduces the difference between predicted and experimental detector densities, the effects of any physical and numerical errors introduced by the model's assumptions within the final reconstruction can be reduced.

2. Model-driven reconstruction workflow

The overall workflow that will be undertaken when performing this new model-driven reconstruction protocol is shown in figure 1. Here, all the different core algorithm components are highlighted. The model initialisation step (purple) involves defining the initial specimen structure (geometry) from prior experimental data such as electron tomography, as well as initial guesses for model parameters. In this work, such parameters will include the phase evaporation fields and specimen alignment with respect to the detector. The simulated

evaporation of this model and calculation of its charged optics (yellow) will then be performed, closely matching the model in our previous study [7]. Next model calibration (green) will be performed by comparing the similarity of the model's predictions back to the experimental data. By feeding this similarity measurement back into the model parameter initialisation, the evaporation model can be optimised to best match experiment. Finally, an optional postprocessing step (red) can further relax the charged optics constraints imposed by the evaporation model's assumptions. The result is a final calibrated reconstruction that has been optimised to best match our initial knowledge of the specimen structure and evaporation physics.

3. Theory and implementation

In order to drive this new reconstruction protocol, both a physical model for field evaporation, as well as an approach for calibrating this model to experimental data is required. The theory and methodology behind these will be covered in the following section. Further details on the continuum modelling framework, code implementation, and choice of parameters can be found in our previous publications [6, 7].

3.1. The continuum evaporation model: a summary

This subsection summarises the continuum model previously developed [7], which will drive the reconstruction protocol outlined in this work. At a particular model time t, the specimen surface local evaporation rate (R_e) can be well described by the Arrhenius law in equation (1):

$$R_e\big(\mathbf{s}(t)\big) = A e^{-\frac{C}{k_B T(\mathbf{s}(t))}\left(1 - \frac{\|\mathbf{E}(\mathbf{s}(t))\|}{F_0(\mathbf{s}(t))}\right)} \tag{1}$$

$$F_R = \max_{\mathbf{s}(t) \in \Gamma(t)} \left(\frac{q(\mathbf{s}(t))}{F_0(\mathbf{s}(t))}\right) = 1 \tag{2}$$

Here $\mathbf{s}(t) \in \Gamma(t)$ is a point on the specimen surface ($\Gamma(t)$), $\|\mathbf{E}(\mathbf{s})\|$ is the local surface electric field strength, $F_0(\mathbf{s})$ is the local material-dependent evaporation field, $T(\mathbf{s})$ is the surface temperature, and k_B is the Boltzmann constant, and C and A are model constants. At present, the model assumes individual phases are of a uniform evaporation field. Here the C term has been assumed constant, and assigned a typical value of 1.3 eV [13]. In this work, the temperature T has also been assumed constant over the surface ($T = 50$ K). It should be noted that these assumptions (in particular that of a constant temperature field) will likely have some effect on the generated reconstructions shown later in this study. A constant $F_R = 1$ field reduction factor has also been maintained. As A is a global constant, its value does not effect the evolution of Γ itself, only the solution's time parameterisation.

Throughout the simulation, the specimen surface (Γ) is embedded as the zero contour within a three-dimensional scalar field (ϕ), as given by equation (3). This field is initialised to be a signed distance field.

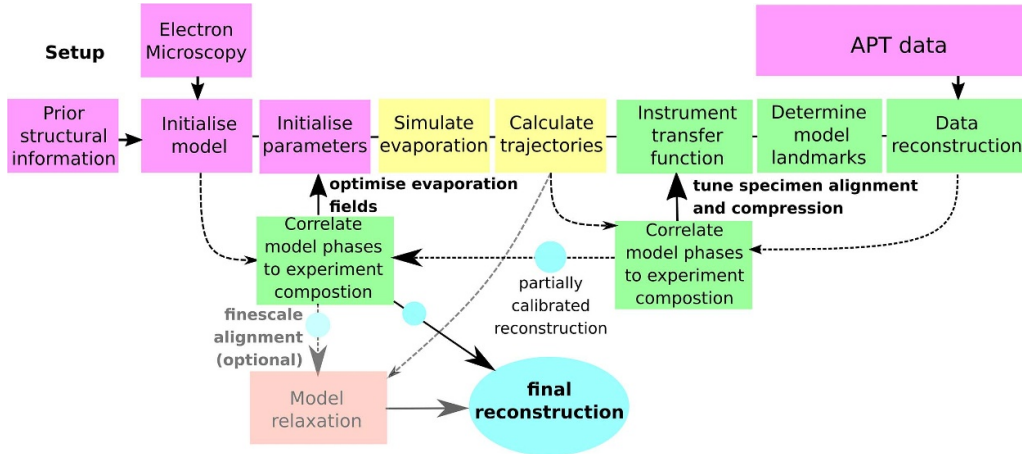$$\Gamma(t) = \{\mathbf{x} \mid \phi(\mathbf{x}, t) = 0\}. \tag{3}$$

Figure 1. Outline for the proposed complete reconstruction workflow. The coloured regions break down the workflow into various blocks. Arrows imply the flow of data.
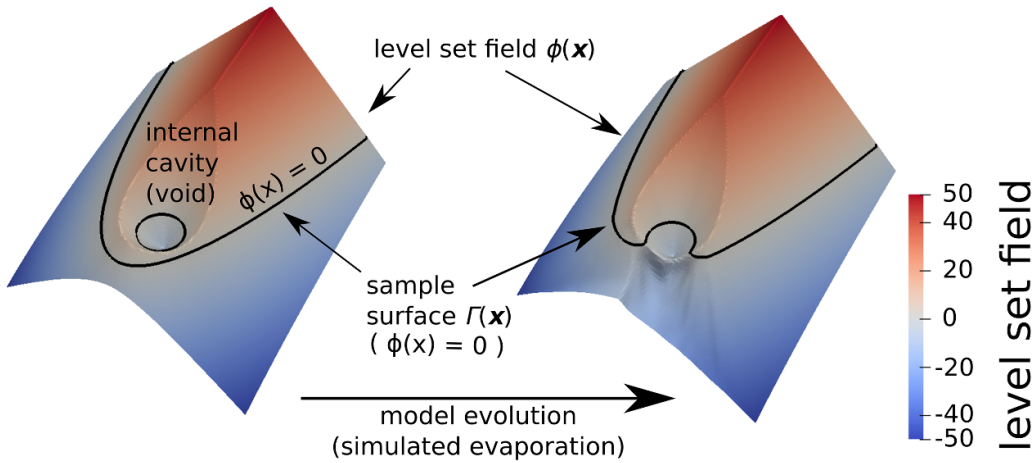

Figure 2. Diagram showing how a specimen containing a void (its surface given by the black curve) is embedded as the zero contour in the scalar field $\phi(\mathbf{x})$. This visualisation was generated using our 2D model [6].

The embedded specimen surface (figure 2(a)) is then evaporated by evolving $\phi(\mathbf{x},t)$ under the level set equation (equation (4)):

$$\frac{\partial \phi(\mathbf{x},t)}{\partial t} - \nu(\mathbf{x},t)\|\nabla \phi(\mathbf{x},t)\| = 0, \qquad (4)$$

here $\nu(\mathbf{x},t)$ is the velocity extension field. For a particular time t, this velocity field is calculated by extending the surface evaporation rate defined at the surface interface (Γ) throughout the level set simulation domain (Ω) according to equation (5):

$$\nu(\mathbf{x},t) = -R_e(\mathbf{s}_m(t)) \quad \text{where} \quad \mathbf{s}_m(t) = \operatorname*{arg\,min}_{\mathbf{s}(t)\in\Gamma(t)} \|\mathbf{x} - \mathbf{s}(t)\|. \qquad (5)$$

To prevent significant drift of ϕ from a signed distance field, the reinitialisation scheme described by Sussman *et al* [14] is performed every 50 iterations by solving equation (4).

Like our previous study [7], electric fields are approximated under electrostatics via a boundary element method (BEM),

with the specimen assumed to behave as a conductor under the high electric fields present. Under the conductor approximation, the electric field in the problem domain surrounding the specimen is given by Laplace's equation in equation (6). At the surface of a conductor, the field magnitude equals the surface normal field flux, i.e. $q(\mathbf{s}) = \mathbf{E}(\mathbf{s})\cdot\mathbf{n}(\mathbf{s}) = \|\mathbf{E}(\mathbf{s})\|$. Thus, $q(\mathbf{s})$ can be used directly to calculate the evaporation rate in equation (1):

$$\begin{aligned} \nabla^2 u(\mathbf{x}) &= 0 & \mathbf{x} &\in \mathbf{X}^-(t) \\ u(\mathbf{s}) &= V(t) & \mathbf{s} &\in \Gamma(t), \end{aligned} \qquad (6)$$

here $\mathbf{X}^-(t)$ is the electrostatic problem domain outside of the specimen (the vacuum). Following discretisation, the specimen surface can be represented by k triangular surface panels ($\Gamma_j \subset \Gamma$), where $\Gamma = \bigcup_{j=1}^k \Gamma_j$. Each panel Γ_j is then given an associated constant potential (u_j) and normal flux (q_j). Following this boundary discretisation scheme, the surface electrostatics can be calculated through a direct boundary

J. Phys. D: Appl. Phys. **55** (2022) 375301

C Fletcher *et al*

element method by solving the system of linear equations given in equation (7):

$$\sum_j^k F_{ij}u_j = \sum_j^k G_{ij}q_j \qquad \forall i \in \{1,2,\ldots,k\} \qquad (7)$$

$$G_{ij} = \frac{1}{4\pi}\int_{\Gamma_j}\frac{1}{\|\mathbf{x_i}-\mathbf{y}\|}d^2\mathbf{y} \qquad (8)$$

$$F_{ij} = \frac{1}{4\pi}\int_{\Gamma_j}\frac{(\mathbf{x_i}-\mathbf{y})\cdot\hat{\mathbf{n}}_j}{\|\mathbf{x_i}-\mathbf{y}\|^3}d^2\mathbf{y}, \qquad (9)$$

here $\hat{\mathbf{n}}_j$ is the normal vector and $\mathbf{x}_i$ is the centre node for surface panel Γ_j. Once the electrostatics on the specimen surface have been solved, with each Γ_j now having a determined u_j and q_j, the electric field ($\mathbf{E}(\mathbf{z})$) can be calculated at any point in space outside of the specimen by solving the following boundary integral equations:

$$E_l = \frac{\partial u(\mathbf{z})}{\partial x_l} = \int_{\Gamma}\frac{\partial^2 G(\mathbf{z},\mathbf{y})}{\partial n\,\partial z_l}u(\mathbf{y})d\Gamma(\mathbf{y})$$
$$- \int_{\Gamma}\frac{\partial G(\mathbf{z},\mathbf{y})}{\partial z_l}\frac{\partial u(\mathbf{y})}{\partial n}d\Gamma(\mathbf{y}), \qquad (10)$$

$\forall \mathbf{z}\in\mathbf{X}^-,\ \mathbf{y}\in\Gamma$ and $l\in\{1,2,3\}$ where $\mathbf{E}=(E_1,E_2,E_3)$
$\mathbf{z}=(z_1,z_2,z_3)$

The calculation of equation (10) is further accelerated via a panel clustering scheme [7]. Finally, ion trajectories from an initial point on the specimen surface ($\mathbf{z}_0\in\Gamma$) can be calculated by integrating the system of first-order equations in equation (11):

$$\begin{bmatrix}\dfrac{d\mathbf{v}}{dt}\\[2mm]\dfrac{d\mathbf{z}}{dt}\end{bmatrix} = \begin{bmatrix}\dfrac{ne}{m} & 0\\[2mm] 0 & 1\end{bmatrix}\cdot\begin{bmatrix}\mathbf{E}(\mathbf{z})\\[2mm]\mathbf{v}\end{bmatrix}, \qquad (11)$$

here m is the ion's mass, $\mathbf{E}(\mathbf{z})$ is the electric field solved via equation (10), ne is its charge, and $\mathbf{v}$ is its instantaneous velocity. It should be noted that assuming an initial velocity of zero, the trajectory taken by an ion is independent of its mass m.

The output is a sequence of specimen surface meshes $\{\Gamma^0,\ldots,\Gamma^t,\Gamma^{t+1},\ldots,\Gamma^f\}$, extracted at each model iteration of equation (4) from $\phi(\mathbf{x})$. Coupled with electrostatic charged optics calculations, it is these model results that will constrain and guide the reconstruction protocol. However, in order to calibrate the parameters of this physics model to an experiment, a new methodology is required. The steps required for performing such a calibration will be outlined in the following sections.

3.2. Instrument transfer function

Up until now, this previously developed physics model has accounted only for the electrostatic field solution resulting from the specimen geometry. While a local electrode can be readily included into the electrostatic solution [15], directly incorporating a biased detector, APT instrument chamber, or a more distant counter electrode poses a significantly greater challenge due to the problem domain's large length-scale differences. These range from the nanometre-scale close to the emitter apex, to ion flight paths covering fractions of a meter.

For the current implementation of the electrostatic solver, a full APT instrument simulation proved impractical. In practice, these additional instrument components introduce further field lensing and compression of ion trajectories towards the detector, increasing the experiment field-of-view (FOV). Therefore, a correcting function must be applied to calculated trajectories in order to compensate for this.

In this work a linear projection law, similar to that in [16], has been assumed to describe ion trajectories on passing a certain distance from the specimen (see figure 3). This projection is performed once ion trajectories have been explicitly calculated via equation (11) up to a set cutoff distance d from the specimen surface. This law introduces an additional compression parameter (κ) that will later be tuned to best match the particular APT experiment being simulated or reconstructed. A suitable value for this cutoff $d = 5\ R_{\mathrm{apex}}$, was determined by investigating the effect of specimen surface protrusions and concavities on the surrounding electric field with distance from the surface (see section I in the supplementary material).

3.3. The trajectory mapping

Previous studies have introduced the concept of defining a trajectory mapping [6, 7, 17, 18]. At an instant in time, this mapping describes how initial launch positions on the specimen surface correspond to final impact positions on the detector (e.g. $\Gamma \to \mathbb{R}^2$). Critically, by considering the stability of equation (11) under changes to an ion's initial launch position, it is possible to show that this mapping is continuous (a proof for which is outlined in [15]). This allows for an estimation of the trajectory mapping to be constructed from the interpolation of ion trajectories uniformly sampled over the specimen surface.

Assuming that no changes in specimen surface topology occur (e.g. the evaporation of voids [19, 20]), this trajectory data can be interpolated between model surface iterations (e.g. Γ^t and $\Gamma^{t+\gamma}$), enabling a time-dependent trajectory mapping ($\mathcal{T}:\mathbb{S}\to\mathbb{D}$) to be constructed between the original material sample space ($\mathbb{S}=\mathbb{R}^3$), and the detector space ($\mathbb{D}=\mathbb{R}^2\times\mathbb{N}$). Under this definition, for a particular ion with initial launch coordinates $\mathbf{x}_l$ and final detector coordinates $\mathbf{x}_d$, the true trajectory mapping yields $\mathcal{T}(\mathbf{x}_l)=\mathbf{x}_d$. The process of data reconstruction then falls down to deriving an estimate for the inverse of this mapping $\mathcal{R}^{-1}\approx\mathcal{T}^{-1}$.

For the implementation in this work, when constructing this inverse mapping ($\mathcal{R}^{-1}$), a bijective assumption has to be currently assumed. Ions are launched from the corner points of the triangular surface panels, their trajectories calculated up to the detector (under the transfer function in section 3.2), and their final impact positions on the detector recorded. The
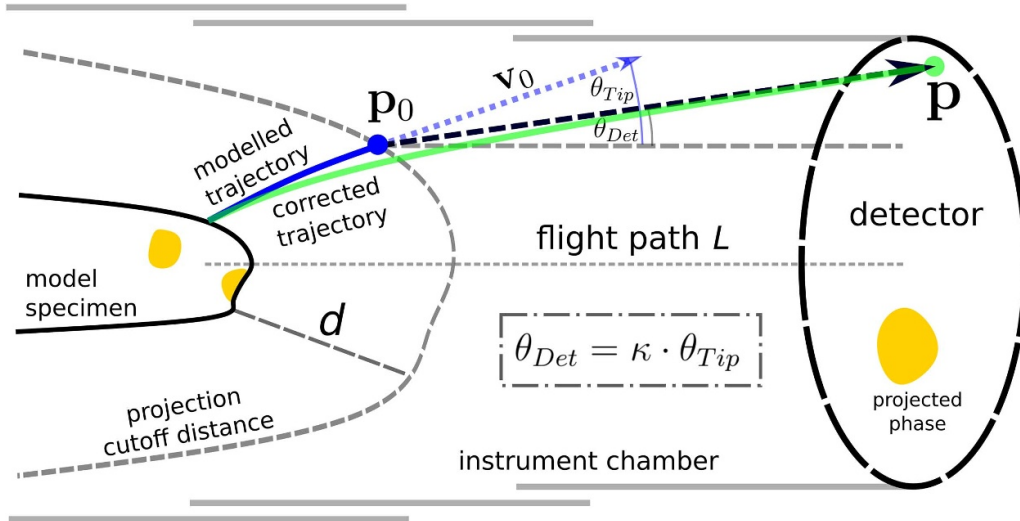
J. Phys. D: Appl. Phys. **55** (2022) 375301

C Fletcher *et al*

Figure 3. The geometric setup for the linear transfer projection. Ion trajectories are calculated up to a distance (*d*) from the specimen surface (terminating at the cutoff distance $\mathbf{p}_0$), with a final velocity vector of $\mathbf{v}_0$. Beyond this, a linear law projection is performed (see boxed equation) up to the detector plane (the green point) to account for any instrument trajectory compression.

inverse mapping at model surface states where trajectories are calculated can then be constructed by interpolating these initial ion launch positions with respect to their final detected positions onto a uniform detector grid (see figure 4). This is performed through triangulation of the final detected positions, followed by barycentric interpolation. The result is a stack of detector grids that each define the state of the inverse mapping at a different point during the simulation. By assigning detector space depth coordinates to each of these detector grids through a calibration method to be described in section 3.4.5, these detector grids can then be interpolated over the entire detector space domain to estimate $\mathcal{R}^{-1}$. Note that this mapping only considers the initial and final ion coordinates, with specific trajectory details during ion flight not explicitly required to perform reconstruction. Ion launch velocities are also assumed to be zero. Following this inverse mapping's estimation, detected ions can be uniquely positioned in the reconstruction.

3.4. Charged optics

In order to compare the evaporation model and calculated trajectory mapping with experiment, synthetic ion detection data must be calculated. Whilst it has been previously shown how comparable data can be generated randomly via a Monte Carlo sampling approach [7], a significantly more efficient method is outlined here that considers the predicted evaporating ion flux from each panel, and its transformation onto the detector under the derived mapping. This more efficient method is one of the key steps required to make model parameter optimisation computationally tractable.

3.4.1. Model state subsampling. Due to the continuity properties of ion trajectories outlined in section 3.3, ions will not be launched at every model surface iteration, but instead for only a subset of these. In this study, the
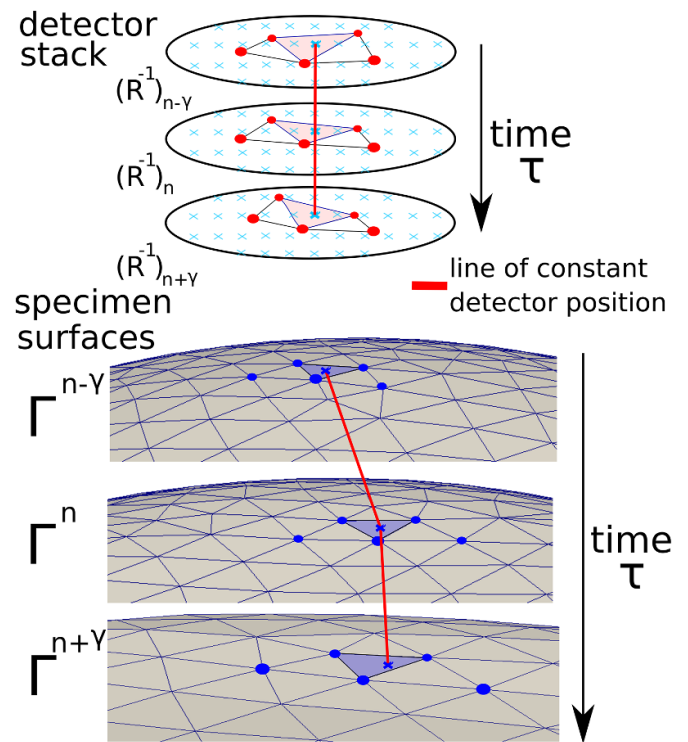

Figure 4. The construction of the temporal inverse mapping $\mathcal{R}_\alpha^{-1}(\tau)$ is shown at a particular detector grid position. The panel this point falls within is highlighted at each model instance. Finally, by interpolation, the corresponding specimen surface position can be derived throughout time (red line).

charged optics will be calculated for the model states at every $\gamma = 5$ iterations, giving the subset of surface meshes $\{\Gamma^0, \ldots, \Gamma^{\gamma \cdot (n-1)}, \Gamma^{\gamma \cdot n}, \ldots, \Gamma^{\gamma \cdot p_f}\}$. Using this subsampled set of states significantly reduces the number of trajectory calculations required, and avoids calculations where only small changes to the modelled specimen surface have occurred.
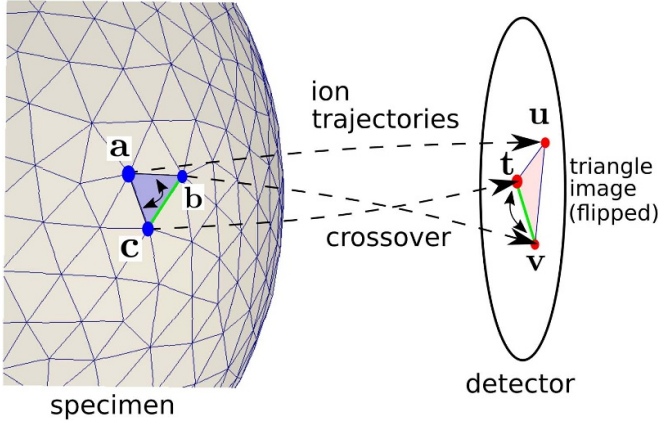
J. Phys. D: Appl. Phys. **55** (2022) 375301

C Fletcher *et al*

Figure 5. Diagram showing the projection of a surface panel onto the detector. Trajectory crossover results in the projected panel inverting (flipping).

For the following optics calculations, the volume of locally evaporated material between these surface states will be required. In this work, we approximate the local volume of evaporated material ($\omega_{\Gamma_i^{\gamma \cdot n}}$) over a surface panel $\Gamma_i^{\gamma \cdot n}$ between the surface states $\Gamma^{\gamma \cdot n}$ and $\Gamma^{\gamma \cdot (n-1)}$ via equation (12):

$$\omega_{\Gamma_i^{\gamma \cdot n}} = \min_{\mathbf{s}' \in \Gamma^{\gamma \cdot (n-1)}} \|\mathbf{x}_i - \mathbf{s}'\|, \tag{12}$$

with the subset of model states defined for which charge optics calculations will be performed, and the local volume of evaporated material from surface panels determined, various properties of the charged optics and simulated data detection can now be calculated.

3.4.2. Local magnification. Previous studies have introduced the concept of APT specimen magnification and local magnification [21–25]. Here, the authors propose formalising this concept of local surface magnification through the local Jacobian (**J**) of the trajectory mapping. In particular, a useful signed scalar magnification definition can be obtained from the local Jacobian determinant in equation (13). Here, a negative sign for $\|\mathbf{J}\|$ implies that the projected panel has flipped under the trajectory mapping (figure 5). Due to the continuity of the trajectory mapping (see section 3.3), the projection of this negative region onto the detector indicates the region in which spatial trajectory overlap is occurring:

$$\|\mathbf{J}\| = \begin{vmatrix} \dfrac{\partial d_x}{\partial x_t} & \dfrac{\partial d_x}{\partial y_t} \\ \dfrac{\partial d_y}{\partial x_t} & \dfrac{\partial d_y}{\partial y_t} \end{vmatrix}. \tag{13}$$

In order to calculate this magnification for a particular panel Γ_j with corner points $(\mathbf{a}, \mathbf{b}, \mathbf{c})$, projected points onto the detector $(\mathbf{u}, \mathbf{v}, \mathbf{t})$, and an outer normal $\hat{\mathbf{n}}$, a local coordinate system tangential to this panel (see figure 6) is defined through the Gram–Schmidt process via equation (14):
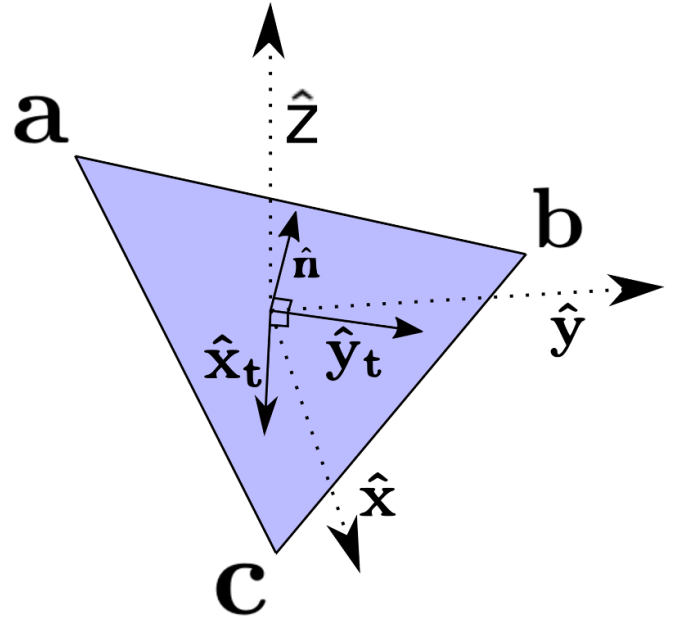

Figure 6. Diagram showing the local tangential coordinate system $(\hat{\mathbf{x}}_t, \hat{\mathbf{y}}_t)$ on a surface panel with normal $\hat{\mathbf{n}}$, with respect to a global coordinate system $(\hat{\mathbf{x}}, \hat{\mathbf{y}}, \hat{\mathbf{z}})$.

$$\begin{aligned} \hat{\mathbf{n}} &= \frac{(\mathbf{b} - \mathbf{a}) \times (\mathbf{c} - \mathbf{a})}{\|(\mathbf{b} - \mathbf{a}) \times (\mathbf{c} - \mathbf{a})\|} \\ \hat{\mathbf{x}}_t &= \frac{\hat{\mathbf{x}} - (\hat{\mathbf{x}} \cdot \hat{\mathbf{n}})\hat{\mathbf{n}}}{\|\hat{\mathbf{x}} - (\hat{\mathbf{x}} \cdot \hat{\mathbf{n}})\mathbf{n}\|} \\ \hat{\mathbf{y}}_t &= \frac{\hat{\mathbf{y}} - (\hat{\mathbf{y}} \cdot \hat{\mathbf{n}})\hat{\mathbf{n}} - (\hat{\mathbf{y}} \cdot \hat{\mathbf{x}}_t)\hat{\mathbf{x}}_t}{\|\hat{\mathbf{y}} - (\hat{\mathbf{y}} \cdot \hat{\mathbf{n}})\hat{\mathbf{n}} - (\hat{\mathbf{y}} \cdot \hat{\mathbf{x}}_t)\hat{\mathbf{x}}_t\|}, \end{aligned} \tag{14}$$

here $\hat{\mathbf{x}} = (1, 0, 0)$ and $\hat{\mathbf{y}} = (0, 1, 0)$ are unit vectors spanning the lateral plane in the global coordinate system. By generating the local panel coordinate systems with respect to this global system, the specific calculated matrix elements of **J** can also be directly compared between surface panels.

The local Jacobian matrix for a panel can then be calculated via equations (15) and (16) [26]:

$$\begin{aligned} b'_x &= (\mathbf{b} - \mathbf{a}) \cdot \hat{\mathbf{x}}_t & c'_x &= (\mathbf{c} - \mathbf{a}) \cdot \hat{\mathbf{x}}_t \\ b'_y &= (\mathbf{b} - \mathbf{a}) \cdot \hat{\mathbf{y}}_t & c'_y &= (\mathbf{c} - \mathbf{a}) \cdot \hat{\mathbf{y}}_t \end{aligned} \tag{15}$$

$$\mathbf{J}^T = \frac{1}{2A} \begin{pmatrix} b'_y - c'_y & c'_y & -b'_y \\ c'_x - b'_x & -c'_x & b'_x \end{pmatrix} \cdot \begin{pmatrix} u_x & u_y \\ v_x & v_y \\ t_x & t_y \end{pmatrix}, \tag{16}$$

here $\mathbf{b}' = (b'_x, b'_y)$, $\mathbf{c}' = (c'_x, c'_y)$, $\mathbf{u} = (u_x, u_y)$, $\mathbf{v} = (v_x, v_y)$, $\mathbf{t} = (t_x, t_y)$, and A is the original panel area on the specimen surface.

Using this definition, we can now calculate $\|\mathbf{J}\|$ over the specimen surface, and also consider its projection under the trajectory mapping onto the detector. An example of this is shown for a surface concavity in figure 7. Figure 7(a) shows the local magnification over the surface (showing the surface region with panel flipping in blue), whilst figure 7(b) shows the projection of these magnification values onto the detector.
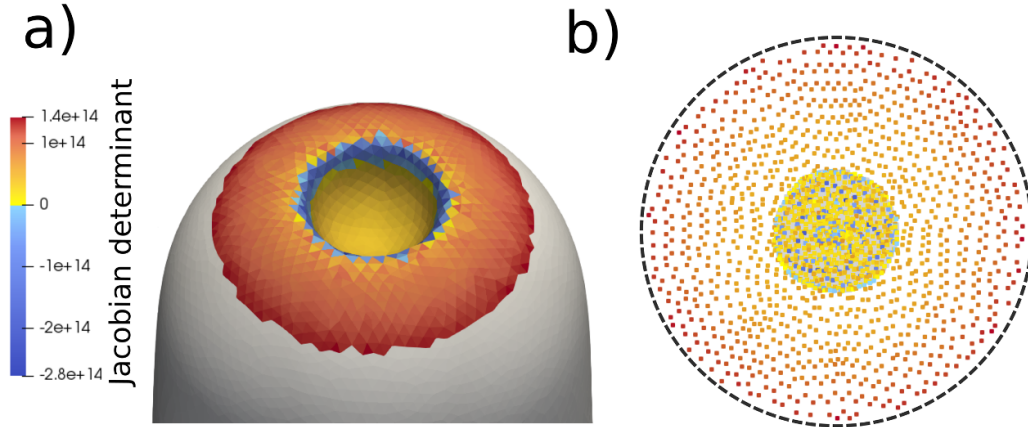
Figure 7. (a) Local panel magnification on the specimen surface featuring a concavity. Blue points indicate a local image inversion. (b) Corresponding image of local stabilities following projection onto the detector. Spatial mixing of positive (yellow) and negative (blue) projected panel stabilities indicates that trajectory overlap is occurring within the grey shaded region.
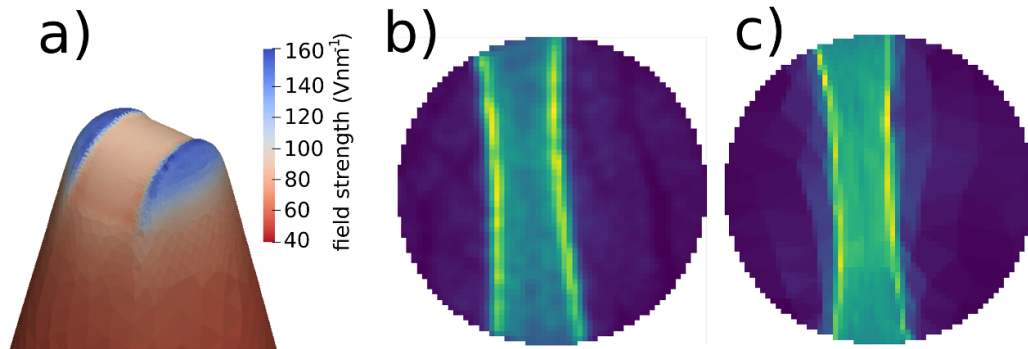

Figure 8. (a) The model surface that ions are launched off. (b) Gaussian-smoothed density hitmap simulation by an MC approach (95 681 ions launched in 19 min 10 s). (c) Density hitmap simulation via the flux method (calculated in 3.6 s).

The detector region in darker grey shows where panel flipping is occurring, and where subsequently the inverse trajectory mapping becomes multivalued due to the presence of trajectory crossover.

3.4.3. Detector density hitmap calculation. In our previous work, we used a Monte-Carlo method to simulate the evaporation events from the surface mesh. For a realistic ion count, this approach is extremely time consuming. In this work, we switch to a method which directly transfers the ionic flux from the surface onto the detector via the Jacobian determinant.

Now that the local magnification has been determined for each surface panel, the hit density ($\langle \rho_d \rangle_B$) averaged over some detector region B can be estimated via the summing of panels' evaporating ion fluxes in equation (17):

$$\langle \rho_d \rangle_B = \frac{1}{A_B} \sum_i^{\Gamma^n} \omega_{\Gamma_i^n} \cdot \left| \|\mathbf{J}\|_i \right|^{-1} \cdot A_{\mathcal{R}(\Gamma_i^n) \cap B}, \qquad (17)$$

here A_B is the area of the averaging region on the detector, $\omega_{\Gamma_i^n}$ is the volume of locally evaporated material over panel Γ_i^n, and $A_{\mathcal{R}(\Gamma_i^n) \cap B}$ is the intersection area between the projection of panel Γ_i^n and B. Computationally, this area is calculated by determining its bounding polygon of the intersection through

the Cohen-Sutherland line clipping algorithm [27]. By evaluating equation (17) for each detector grid cell, the detector density hitmap can be constructed at a particular model surface state (figure 8).

This calculation of a detector density hitmap with N_D grid cells can also be described by the rectangular $k \times N_D$ linear system in equation (18). Here $\omega_{\Gamma_j^n} \in \boldsymbol{\omega}$ is the k-length vector of local panel evaporation volumes, and $(\langle \rho_d \rangle_{B_i})_i \in \boldsymbol{\rho}$ is the N_D-length vector of detector densities. It should be noted that this matrix equation can be inverted, potentially allowing for the back-projection of detector hitmap densities onto the specimen surface. In this case, a sufficiently high resolution detector discretisation should be used to ensure the system is not underdetermined:

$$\mathbf{M} \cdot \boldsymbol{\omega} = \boldsymbol{\rho} \qquad \text{where } M_{ij} = \frac{1}{A_{B_i}} \left| \|\mathbf{J}\|_j \right|^{-1} \cdot A_{\mathcal{R}(\Gamma_j) \cap B_i}. \quad (18)$$

Now that the detector density hitmaps can be determined for particular model surface states, a representation of the predicted ion density throughout a simulation's detector space can be obtained. This information is critical for calibrating the depth positioning of ions in the model-driven reconstruction protocol to be outlined in section 3.5.
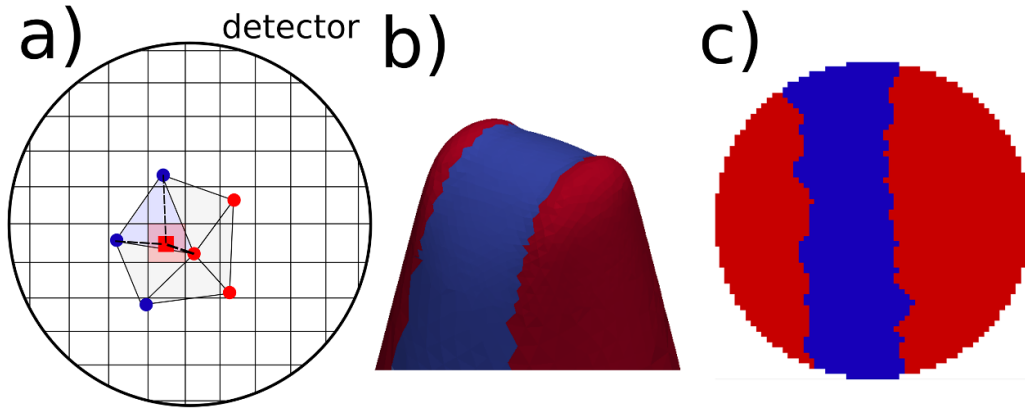
J. Phys. D: Appl. Phys. **55** (2022) 375301

C Fletcher *et al*

Figure 9. (a) Nearest-neighbour interpolation of projected phases onto the detector grid. (b) Specimen surface showing local material phase for a particular model state. (c) Its corresponding predicted local detector phase map.

3.4.4. Detector phase map calculation. As with the local detector density, the local detector phase can also be determined. Knowledge of the local model phase throughout the simulated detector space will prove a critical metric for assessing the similarity between a particular model and the experimentally measured composition (see section 3.6.2).

A particular model phase can be assigned to each panel through a point-in-polygon test of panel centres with the internal phase meshes. The projection of these panel centres under the trajectory mapping is then considered, with local phase calculated via nearest-neighbour interpolation of these panel centres over the discretised detector grid (illustrated in figure 9(a). An example detector phase map for a particular model state (figure 9(b)) is shown in figure 9(c).

3.4.5. Detector space interpolation. Now that the evaporation rate can be efficiently calculated throughout the simulation, for each model surface state from which trajectory calculation is performed, e.g. $\Gamma^{\gamma \cdot l}$, a depth position in detector space $(z_{\mathrm{d}}^{\gamma \cdot l})$ can be assigned via equation (19):

$$z_{\mathrm{d}}^{\gamma \cdot l} = -\eta \sum_{n=0}^{l} \frac{\sum_{i=1}^{N} \langle \rho \rangle_{B_i}^{\gamma \cdot n}}{\nu_{\mathrm{ion}}^{\gamma \cdot n}} \quad \text{for } n, l \text{ from}$$
$$\times \{\Gamma^0, \Gamma^{\gamma \cdot 1}, \dots, \Gamma^{\gamma \cdot n}, \dots, \Gamma^{\gamma \cdot l}, \dots \Gamma^{\gamma \cdot p_f}\}, \quad (19)$$

here η is the detection efficiency, and $\{\Gamma^0, \Gamma^{\gamma \cdot 1}, \dots, \Gamma^{\gamma \cdot n}, \dots, \Gamma^{\gamma \cdot l}, \dots \Gamma^{\gamma \cdot p_f}\}$ is the subset of model states from which ion projection was performed (assuming projection is performed every γ surface iterations). The term $\nu_{\mathrm{ion}}^{\gamma \cdot n}$ is the ionic volume associated with model iteration $\Gamma^{\gamma \cdot n}$. The current protocol assumes these ionic volumes to be independent of species type, although future protocols could incorporate species-specific variation. Instead, these ionic volumes are considered to vary with model iteration due to the depth landmarking procedure, initially discussed in [7] to match the depth positions of reconstructed microstructure with their depth positions in the model. The details of the landmarking procedure will be further discussed in section 3.5.

Following assignment of these depth positions, there is now a stack of detector hitmaps (either density or phase) positioned

at various detector space depths $z_{\mathrm{d}}^{\gamma \cdot l}$. These hitmaps can now be spatially interpolated throughout the entire 3D detector space volume to give a 3D voxel field defining the inverse trajectory mapping $(\mathcal{R}^{-1})$, local density $(\mathcal{M}_\rho)$, and local phase $(\mathcal{M}_p)$ throughout the detector space.

3.5. The reconstruction protocol

Now that the inverse trajectory mapping can be constructed, the model-driven reconstruction protocol can be outlined. For a particular detected ion with specific detector coordinates (x_d^i, y_d^i) and evaporation sequence position (z_d^i), the ion can be positioned in the reconstruction using the interpolated inverse mapping, i.e. via $(x_r^i, y_r^i, z_r^i) = \mathcal{R}^{-1}(x_d^i, y_d^i, z_d^i)$. By placing each ion according to this function, the reconstruction can then be constructed. Note that as $\mathcal{R}^{-1}$ is pre-calculated, this placement of ions can be performed in parallel.

However, prior to this ion placement, the depth calibration of model states must be performed through the depth landmarking process described in section 3.4.5. This is required to constrain the values of $\nu_{\mathrm{ion}}^{\gamma \cdot n}$ required by equation (19). During depth landmarking, iteration-specific values for $\nu_{\mathrm{ion}}^{\gamma \cdot n}$ are determined to ensure that the 'top' and 'bottom' of a particular microstructure within the generated reconstruction will align in depth with its corresponding microstructure in the model (see figure 10). This alignment prevents the propagation of modelling errors from causing the model surface to drift in depth away from the true experiment specimen shape over the analysis time. This depth landmarking is performed in detector space, by considering the model iteration (S) when a phase either appears or disappears from a phase map (section 3.4.4), and matching this particular iteration to the ion sequence position (I^S) when the corresponding phases appears or disappears from the experiment hitmap. The ionic volume $(\nu_{\mathrm{ion}}^{S \to S+\gamma \cdot l})$ to use between two model iteration landmarks S and $S + \gamma \cdot l$ to ensure this microstructural alignment can then be determined via equation (20):

$$\nu_{\mathrm{ion}}^{S \to S+\gamma \cdot l} = \eta \frac{\sum_{n=S/\gamma+1}^{S+\gamma \cdot l} \sum_i^N \rho_{B_i}^{\gamma \cdot n}}{I^{S+\gamma \cdot l} - I^S}. \quad (20)$$

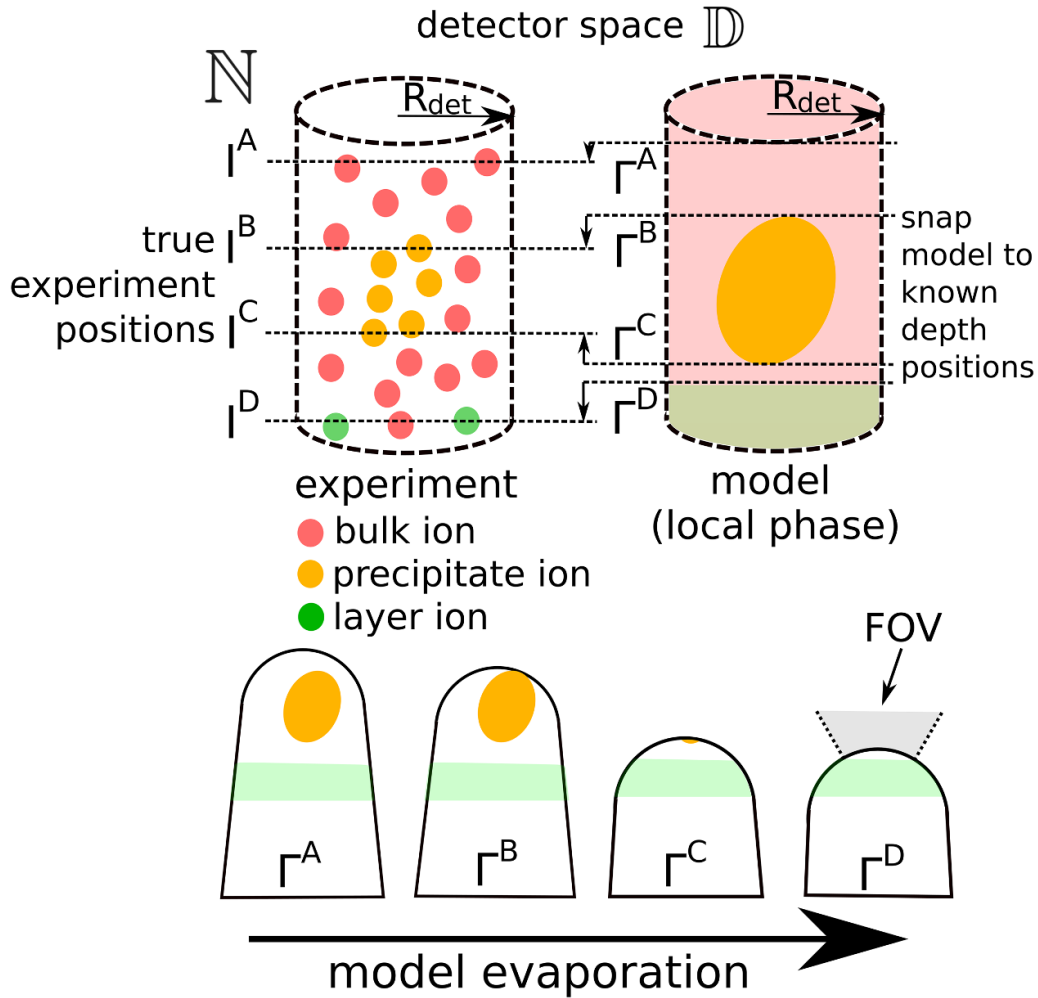J. Phys. D: Appl. Phys. **55** (2022) 375301

C Fletcher *et al*

Figure 10. Diagram outlining the landmarking procedure. Landmarked detector space depth positions are aligned to corresponding model states by selecting appropriate ionic volumes (ν_{ion}^i) for states between landmarks. Particular model states (simulation times) correspond to constant depth slices of detector space.

Once calculated, these ionic volumes allow for the assignment of depth positions for each model surface state, which are applied when interpolating and constructing $\mathcal{R}^{-1}$. Model-driven reconstruction can now be performed between wherever landmarks in detector space have been defined. However, other than ensuring depth alignment, there is currently no guarantee that the model will accurately reflect the dynamics of the experiment, and that the predicted inverse trajectory mapping would improve multiphase distortions over the mapping predicted by conventional projection-based models. Ensuring the accuracy of the model to experiment will require additional calibration of model parameters.

3.6. Reconstruction calibration

Our previous work considered data reconstruction driven by the physics model following a manual tuning of parameters [7]. Here, we outline how this parameter tuning procedure can be automated, through measuring the spatial similarity between the model predictions and experimental composition, as well as how the model's constraints can be partially relaxed to correct for model error.

3.6.1. Parameter optimisation. In order to calibrate the reconstruction, the parameters of the driving model must be optimised under the MI metric (section 3.6.2). In this work, these parameters include the evaporation fields for the various model phases $\mathbf{F}_0 = \{F_0^1, \ldots, F_0^p\}$, as well as the specimen rigid body alignment parameters, and the additional compression parameter (κ) from the linear projection function in section 3.2. A diagram illustrating a particular specimen model's rigid body alignment with respect to the detector is shown in figure 11. In this work, the parameter ϕ is assumed to be zero, reducing the size of the parameter space. This constraint is supported by experiment showing this tilt is frequently only a few degrees, assuming careful specimen mounting in the holder [28]. This leaves the necessary tuning of the model parameters $\mathcal{P} = \mathbf{F}_0$ and alignment parameters $\mathcal{A} = \{\vec{\mathbf{r}}, \theta, \kappa\}$.

The optimisation problem itself can be split up into two stages, reducing the computational workload. This is due to
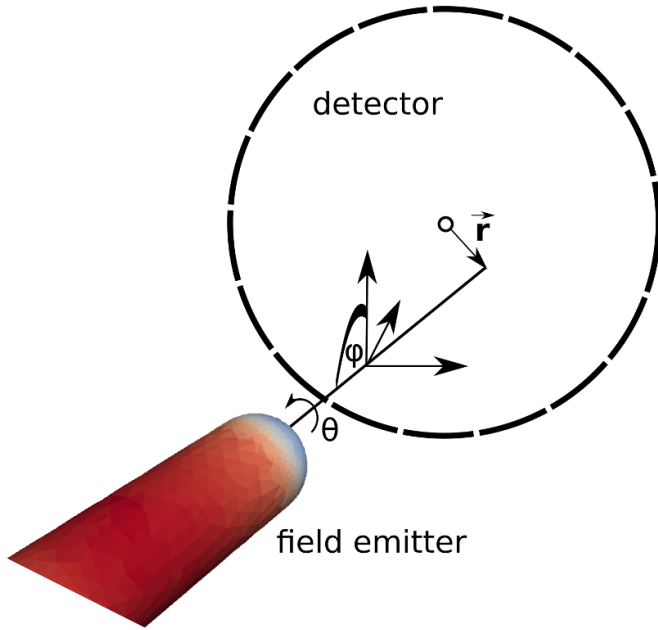
Figure 11. The degrees of freedom in the model spatial alignment with respect to the detector. This includes both translation ($\vec{\mathbf{r}}$) and orientation (ϕ, θ).

only the tuning of $\mathbf{F}_0$ requiring the model to be rerun: a costly operation. Therefore, the model only need be rerun for the optimisation of phase evaporation fields. The alignment parameters can then be tuned via partial optimisation for fixed $\mathcal{P}$. At each parameter optimisation iteration, the similarity in detector space between the predicted model phases and APT experimental composition will be measured. This will be performed through a metric based off Mutual Information (MI) [29].

In this work, only regular and adaptive grid searches have been used when performing the parameter tuning. This is because while local optimisers could more efficiently find a maximum in similarity [30, 31], there is no guarantee that this maximum is global. Indeed, the presence of such local maximum has previously been encountered in studies involving the quantitative calibration of traditional APT reconstructions [12]. In comparison, the results of grid searches can be directly visualised and easily interpreted to determine whether the true maximum has been identified within the explored parameter region. However, there is nothing preventing this optimisation from instead being performed using a method such as Nelder–Mead [31].

3.6.2. Similarity measurement. In order to perform this comparison, a quantitative measure of voxel field similarity must be defined. In this work, the mutual information (MI) metric is considered. Unlike the cross-correlation metric previously considered for reconstruction calibration [11, 12], the MI metric considers the degree of spatial dependence between the model and experimental data. Here, this measurement is performed following voxelisation of both the model and experimental data within detector space on a 3D

grid with dimensions (V_x, V_y, V_z). This yields a model mono-channel image ($\mathcal{M}_p$) corresponding to local phase, and an experiment multichannel image ($\mathcal{E}^c$) corresponding to the local composition of C different ionic species indexed by c. The model image $\mathcal{M}_p$ is generated via the methods outlined in sections 3.4.4 and 3.4.5. In order to measure this mutual dependence, the joint 2D spatial histogram of image voxel intensities ($H^c(\mathcal{M}_p, \mathcal{E}^c)_{i,j}$), as well as the 1D histograms of experiment composition ($H^c(\mathcal{E}^c)_j$) and model phases ($H(\mathcal{M}_p)_i$) must first be determined. In these histograms, a bin count of $N_{\mathcal{M}_p}$ is used along model phase axes equal to the number of unique model phases. An appropriate value for the experimental composition axes bin count ($N_{\mathcal{E}}^c$) has been estimated via Sturges' formula ($N_{\mathcal{E}}^c = 1 + \log_2(V_x \cdot V_y \cdot V_z)$) [32]. The image similarity can then be quantified by the MI definition given in equation (21):

$$S_{MI}(\mathcal{M}_p, \mathcal{E}^c) = \frac{1}{CV_x^2 V_y^2 V_z^2} \sum_c^C \sum_i^{N_{\mathcal{M}_p}} \sum_j^{N_{\mathcal{E}}^c} H^c(\mathcal{M}_p, \mathcal{E}^c)_{i,j}$$

$$\times \log\left(\frac{H^c(\mathcal{M}_p, \mathcal{E}^c)_{i,j}}{H(\mathcal{M}_p)_i \cdot H^c(\mathcal{E}^c)_j}\right) \quad (21)$$

Using this definition, a value of zero implies complete independence, i.e. no correlation, whilst larger values imply increasingly greater correlation between local model phases and experiment composition. As a greater similarity implies a better model fit to the data, at least in the model's ability to predict changes in local phase, the aim is to tune the model's free parameters to maximise this similarity measure ($S_{MI}(\mathcal{M}_p, \mathcal{E}^c)$).

3.7. Model relaxation

The final calibration method to be considered is a fine-scale local model relaxation of the predicted trajectory mapping, aiming to better spatially match the predicted model detector space density signals to those observed in experiment through minor adjustment of the predicted model trajectory data. This relaxation has been applied in an attempt to minimise any residual distortions arising due to remaining model inaccuracies, e.g. errors in the initially assumed specimen geometry, alignment, or evaporation physics. Unlike previous relaxation schemes applied in APT that attempted to homogenise reconstruction densities [33, 34], this approach is applied in detector space ($\mathbb{D}$), maintaining the topological structure of any predicted trajectory crossover regions within the mapping.

In this work, the diffeomorphic density matching algorithm described in [35, 36] is applied between the predicted model detector space ion densities (sections 3.4.5 and 3.4.3), and the experimental detector space ion hit densities (calculated via Kernel Density Estimation [37]) through the *ddmatch* tool [38]. This matching algorithm attempts to determine a smooth and well-behaved function—a diffeomorphism—that best transforms the model density image back onto the experiment density image. These diffeomorphic mapping algorithms are commonly applied in the field of computational anatomy
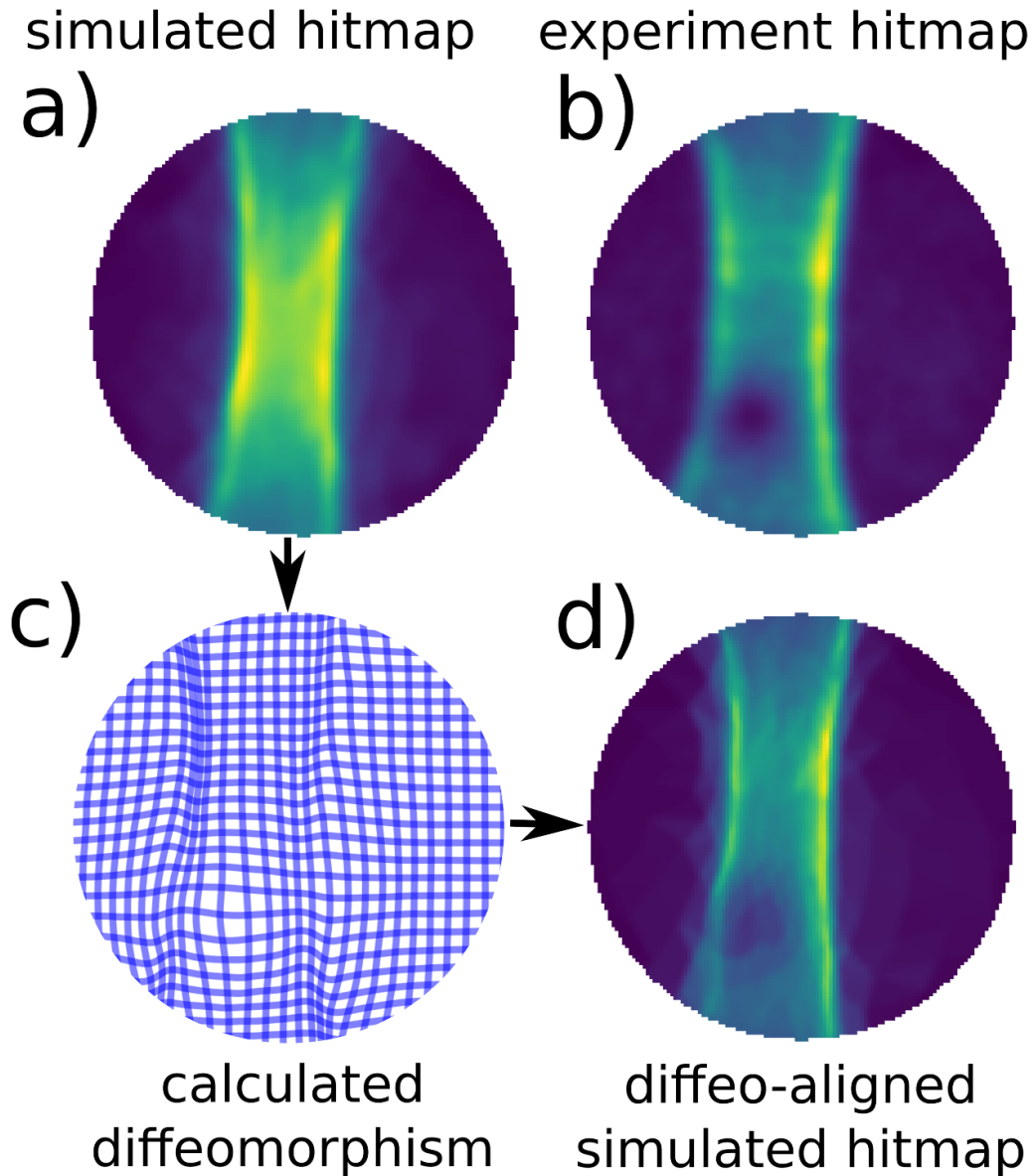
J. Phys. D: Appl. Phys. **55** (2022) 375301

C Fletcher *et al*

simulated hitmap

experiment hitmap

Figure 12. (a) The model density detector map at an instance in time. (b) The experimental density detector map at the same instance (matched together via depth calibration). (c) The determined alignment transformation. (d) The transformed model density detector map. The low density pole has been partially accounted for. Alignment performed using the open-source code *ddmatch* [38].

in order to match a patient's imaged organ structure back to a model [35, 39, 40]. In our case, this algorithm will instead match the evaporation model's ion density predictions back to the experimental APT image data by determining a local matching transformation. This determined local transformation is then applied to the model's trajectory mapping prior to data reconstruction, with the magnitude of the required local matching transformation providing information about the local model error.

The application of the diffeomorphic density matching algorithm implemented in *ddmatch* between a predicted model and experimental density detector hitmap for a fin field-effect transistor (finFET) semiconductor dataset is shown in

figure 12 (further discussed in section 4.2). It can be seen that this algorithm derives a transformation (figure 12(c)) that better aligns the original model predicted hitmap (figure 12(a)) to the experimental hitmap (figure 12(b)). This relaxation of the model transforms the predicted trajectory mapping such that model detector densities (figure 12(d)) better match the experimental data densities (figure 12(b)).

This model relaxation procedure can be applied as an optional postprocessing step within the reconstruction workflow (see figure 1). It appears to be most impactful when applied to materials systems exhibiting large changes in spatial magnification (in particular where there is significant local demagnification).

4. Results and discussion

Through the workflow outlined in figure 1, the reconstruction of experimental APT datasets using the defined evaporation model can be performed. In the following section, the model-driven reconstruction of two semiconductor structures will be considered: a SiGe multilayer system (section 4.1), and a fin field-effect transistor (finFET) device (section 4.2). Both of these will be compared to their conventional point-projection reconstructions under the Bas protocol [3].

For both these following reconstructions, a simulated flight path of $L = 0.102$ m and detector radius of $R_d = 0.038$ m has been used. This configuration matches the LAWATAP instrument on which both these experimental datasets were obtained.

4.1. Reconstruction of a multilayer system

The first material system considered is an SiGe multilayer system. Experimental details for this system can be found within section III of the supplementary material. Prior to analysis, the specimen has been prepared via a gallium FIB. The 3D structure of the specimen surface and internal phases is known from correlative electron tomography (ET), reconstructed via the SIRT algorithm [41] from a tilt series taken in the HAADF-STEM imaging mode prior to APT analysis (figure 13(a)). From the 3D ET voxel field, isosurfaces have been manually extracted for the specimen surface and phases (figure 13(b)). These extracted isosurfaces have then been used to initialise the specimen model (figure 13(c)). It is worth noting that a drop in ET image contrast near the specimen surface prevented an accurate definition of the internal phases in this region. This required extrapolation of the internal layer phases up to the specimen surface. Possible causes for this loss of contrast include ET reconstruction artefacts or material amorphisation due to Ga implantation.

Now that the specimen model geometry has been defined, model-driven reconstruction can be considered. Simulations were performed on a $48 \times 38 \times 133$ level set grid, with cell widths of 1.5 nm. Initially, depth calibration of the APT data against the model must be performed. From the approach outlined in section 3.4.5, values for the ionic volumes are determined to use between these landmarks that ensure this alignment through manual placement of specific landmarks in the experiment ion evaporation sequence (figure 14(b)). For the model, these landmarks' corresponding positions are automatically extracted from when the Ge layers first appear within the model predicted detector space (figure 14(a)), with the local phase on the detector determined via the method in section 3.4.4.

Finally, now that both the initialisation of the model and detector space depth calibration has been performed, model-driven reconstruction of the experimental data can be carried out via the predicted model's trajectory mapping (section 3.3). However, the model parameters, including the phase evaporation fields, trajectory compression, and alignment parameters must be tuned to optimise the MI similarity metric outlined in section 3.6.2. Here a regular grid search has been performed

over the unknown parameters within the FOV ($\{F_{\text{Si}_{0.3}\text{Ge}_{0.7}}$, κ, θ, $\vec{\mathbf{r}}\}$), measuring the local phase-composition similarity between the model and generated reconstruction via the MI metric (see section 3.6.2). This model parameter tuning considered 12 different evaporation field values for $\text{Si}_{0.3}\text{Ge}_{0.7}$, taking a total time of 4 h. The results from this parameter tuning are visualised in figures 15(a)–(d). These show that an optimum set of parameters can be identified, with the resulting optimum model-driven reconstruction shown in figure 15(e). By comparing with its point-projection reconstruction (performed in shank mode with parameters estimated from the ET data and known layer spacing dimensions), it can be seen that given the optimised specimen model, the tilting distortions observed in the phase layers have largely been successfully corrected for within the model-driven reconstruction.

However, it should be noted that some internal distortions of layers remain. These remaining distortions likely arise due to the extracted layers from the ET data not being completely flat to begin with (see section IV in the supplementary material). Indeed, the final quality of the obtained model-driven reconstruction can only be as good as the initial specimen model. Significant challenges are faced by users, particularly those aiming to define the specimen model using correlative ET data, where any error in the initial geometry and landmark placement may greatly effect the achievable reconstruction quality.

The model-driven reconstruction's normalised density spread (the standard deviation divided by the mean) can also be considered as a metric for reconstruction performance, as real material densities are very frequently near homogeneous. Here the density spread has been calculated from voxel density values, obtained by spatially binning the ion data over a $80 \times 80 \times 80$ grid. Here, voxels on the reconstruction edge have been removed to avoid boundary effects. It was found that the normalised density spread was minimised when the microstructural similarity between the model and experiment was maximised (figure 15(a)), even though the local density has not been considered by the MI microstructural optimisation. The calculated normalised density spread for the optimum model-driven reconstruction was 0.24, lower than the value of 0.28 obtained for the calibrated conventional Bas reconstruction. These results provide additional quantitative evidence that the new automated calibration approach is indeed improving reconstruction quality.

By defining an emitter model from ET data of the initial specimen shape prior to evaporation, the proposed model-driven reconstruction has successfully corrected for multiphase tilting distortions within an experimental dataset for this SiGe multilayer structure. However, here the considered structure is largely cylindrically symmetric around the analysis (depth) axis. In the next example, the stability of the new reconstruction protocol will be explored for an asymmetric structure resembling a modern finFET device.

4.2. Reconstruction of a finFET device

While the new reconstruction algorithm successfully corrected for the layer tilting distortions within the SiGe multilayer
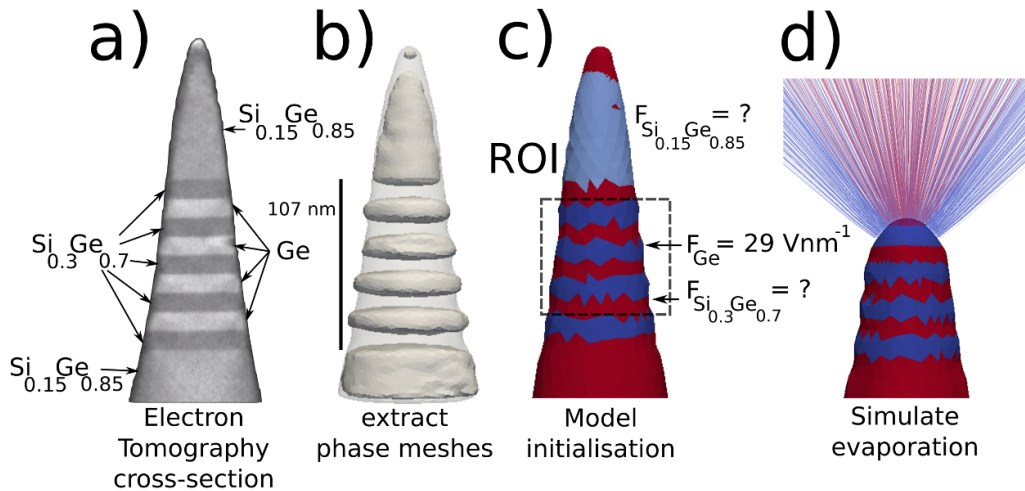
Figure 13. (a) Cross-section of the raw ET data (with background removed). (b) Contour extracted surface and phase meshes. Due to edge contrast loss, phase meshes have been extended to intersect the specimen surface. (c) Initialised model with labelled effective evaporation fields (two unknown). (d) Once these evaporation fields are defined, simulated evaporation of the structure can be performed.
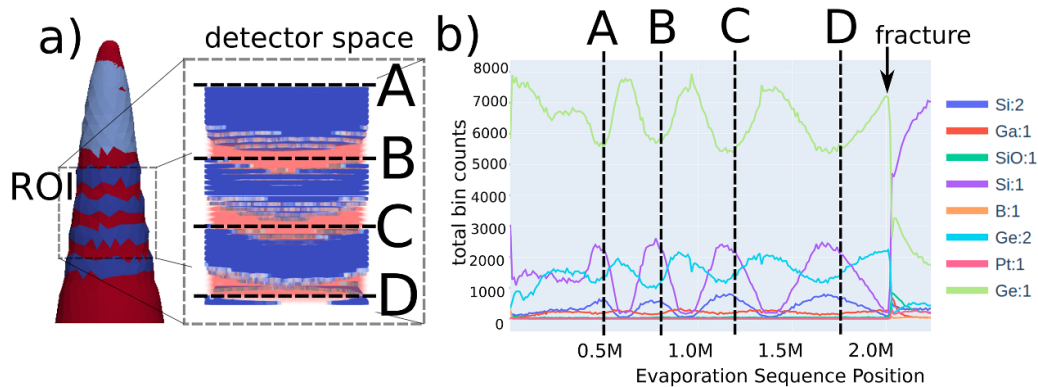

Figure 14. (a) Local phase in the model predicted detector space within the Region Of Interest (ROI). Model landmarks are positioned where Ge (blue) layers enter the FOV. (b) Binned histogram of ion depth positions in detector space, with experimental landmark positions marking the initial evaporation of Ge layers.

dataset, the protocol's stability and performance for non-axisymmetric systems and concave specimen apex shapes has yet to be tested. To investigate this, the protocol was applied to reconstructing an APT dataset for a finFET device. In the authors' previous work [7], this same dataset was 'naively' reconstructed by assuming specific evaporation field values. However, here model alignment, compression, and evaporation field parameters will be automatically selected under the new calibration procedure outlined in section 3.6. Experimental details for the finFET dataset can be found within section III of the supplementary material.

Applying the conventional Bas protocol to the finFET dataset reveals a narrowing distortion and increased density within the central fin region (see figures 16(c) and (d)). This narrowing is not present within the correlative electron micrographs (see figures 16(a) and (b)), implying that the narrowing is likely an APT imaging artefact, due to the differing evaporation mechanics of the SiGe and SiO₂ phases. This differing phase evaporation behaviour results in a specimen apex shape deviating significantly from the assumed hemisphere of the Bas protocol [3, 7, 34].

In order to drive the reconstruction protocol, we must first define the specimen model. Unlike the multilayer system, correlative ET data was unavailable for the finFET dataset. Instead, the model's specimen structure was estimated using prior knowledge of the device geometry and correlative electron micrographs (figures 16(a) and (b)). Using this data, an initial specimen geometry for the evaporation model could be determined as shown in figure 16(h). Further details of the finFET model's initialisation can be found in our previous work [7].

Once the initial model state has been defined, its evaporation can be simulated. For this an $84 \times 84 \times 134$ simulation grid was used, with cell widths of 3 nm. Like with the multilayer system, suitable landmarks must be provided to calibrate the model and experimental detector spaces. The placement of landmarks in the experiment ion evaporation sequence are shown in figure 17. Unlike our previous work [7], the corresponding landmark positions for the model are automatically determined from when particular model phases appear and disappear from the detector phase maps.
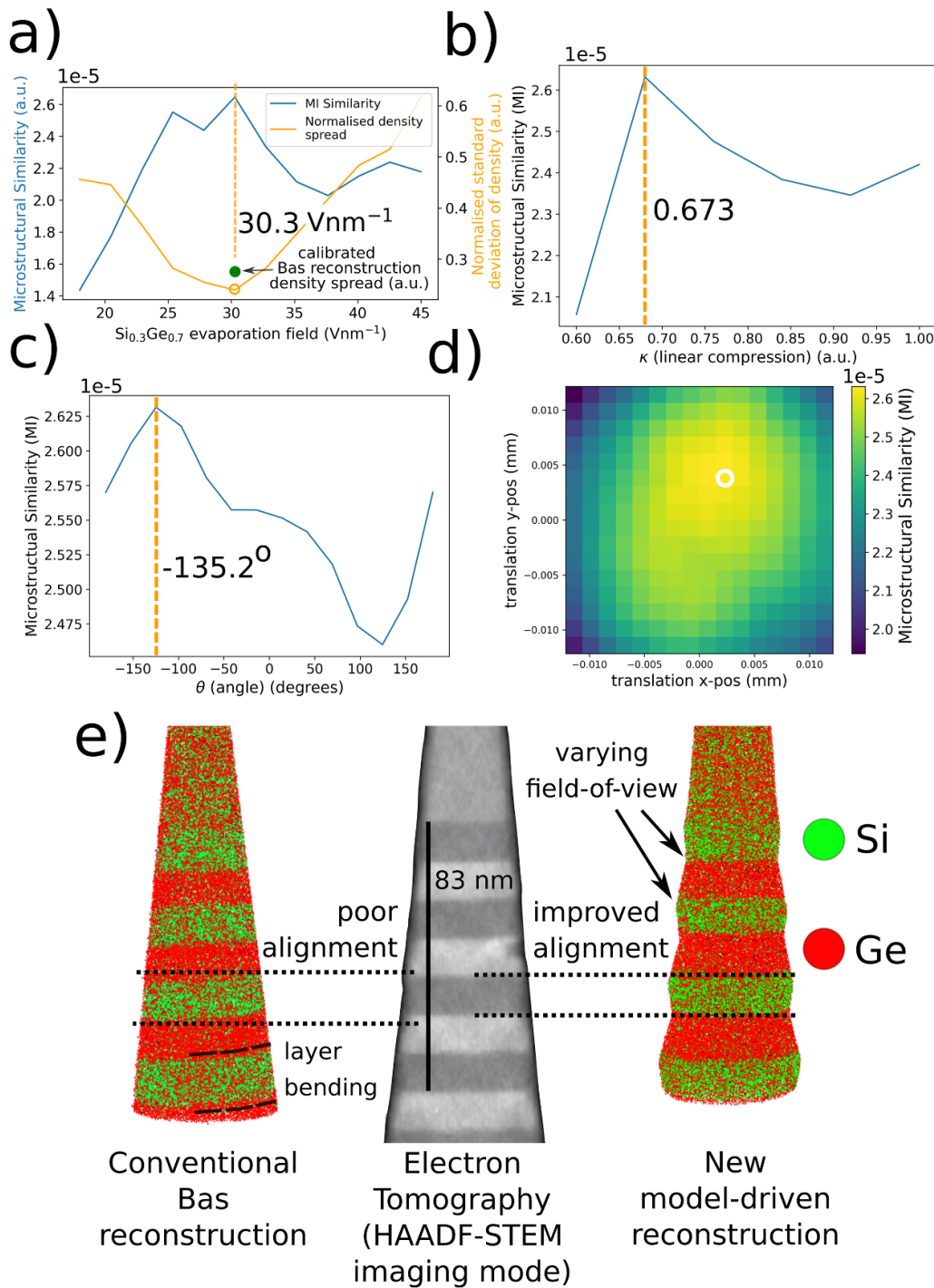
Figure 15. (a) Regular grid search over $F_{\mathrm{Si}_{0.3}\mathrm{Ge}_{0.7}}$ in detector space under the MI metric. (b)–(d) Plots for the partial optimisations over the instrument compression (κ), and rigid body alignment parameters (θ, $\vec{r}$). (e) Comparison between point-projection reconstruction and optimised model-driven reconstruction. The layer tilting distortions present in the Bas reconstruction have been successfully corrected for.

While approximate values are known for the evaporation fields of Si and Ge [42], no such estimates exist for effective evaporation field values for the SiO$_2$ and SiGe phases. Here, both these unknown phase evaporation fields are tuned via a regular grid search (shown in figure 18(a)), exploring 64 different evaporation models and taking 42 h in total. The specimen alignment, orientation and additional trajectory compression have also been tuned in parallel through an adaptive grid search performed over three increasingly fine grids (figures 18(b)–(d)). Unlike the multilayer system, adaptive grid search proved necessary to achieve convergence when performing specimen orientation and alignment for such a non-axisymmetric structure. The calibration procedure successfully identified an optimum model for driving data reconstruction (figure 19(a)), the corresponding parameters for which are labelled in figure 18.
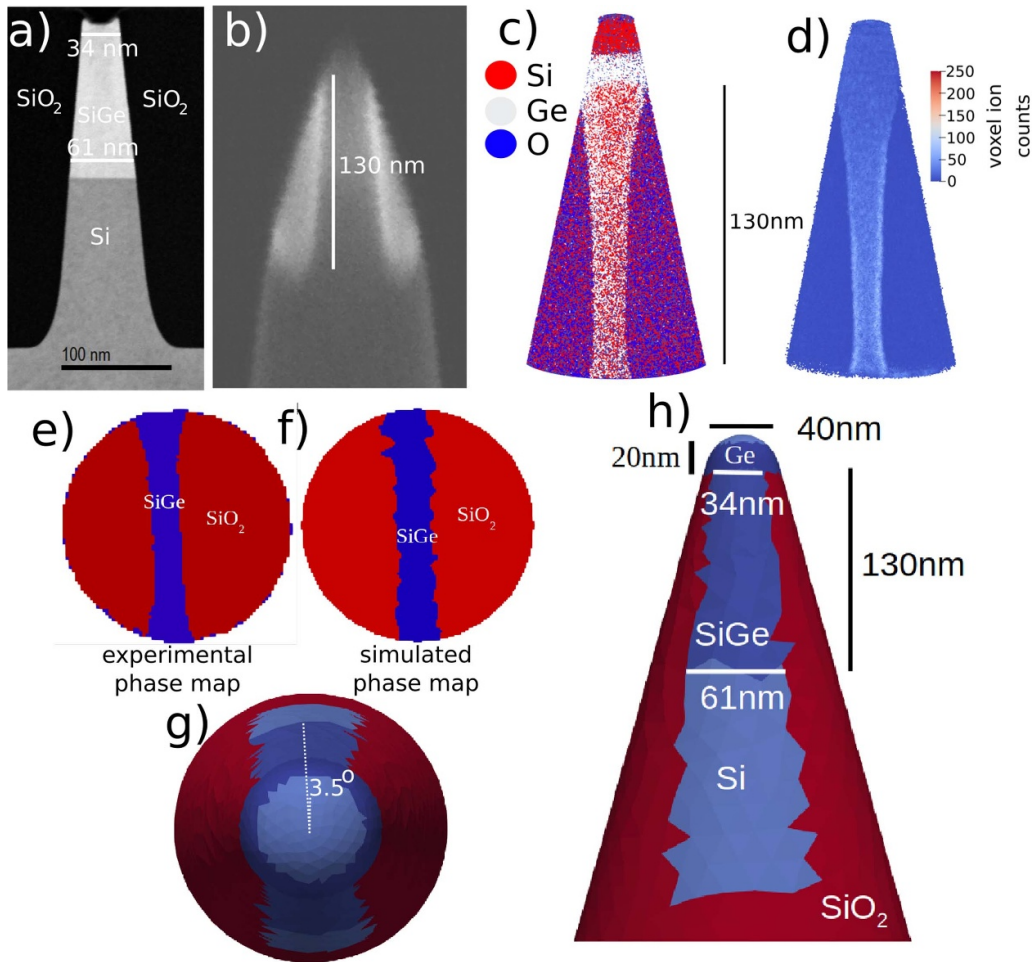
J. Phys. D: Appl. Phys. **55** (2022) 375301

C Fletcher *et al*

Figure 16. (a) DF-STEM imaging of specimen. (b) Denoised SEM image post-milling. (c) Bas reconstruction of APT data showing species. (d) Local density within the Bas reconstruction. (e) Experimental phase map at maximum central fin demagnification. (f) Corresponding model phase map. (g) Top-down view of specimen model showing central fin tilting. (h) Lateral view of FinFET specimen model. As model initialisation remained unchanged from our previous study [7]. Reproduced from [7]. © The Author(s). Published by IOP Publishing Ltd. CC BY 4.0.

While the generated model-driven reconstruction (figure 19(a)) is certainly an improvement over the conventional Bas reconstruction (figures 16(c) and (d)), it can be seen that residual distortions remain at the vertical fin interfaces (see section V in the supplementary material). The presence of these residual distortions is not surprising given both the assumptions made in setting up the model geometry and evaporation physics. However, these distortions can be further reduced by applying the model relaxation step in section 3.7 to the trajectory data of the identified optimum model, just prior to the final data reconstruction. This step aims to calculate a slight correcting transformation to the model trajectory mapping, that when applied better aligns density features in the model predictions and experimental data. The resulting effect on the finFET system's reconstruction is shown in figure 19(b). From this, it can be seen that the relaxation step has successfully reduced the residual bending distortions previously present at the central fin interfaces. The microstructure within the final relaxed reconstruction agrees well with the phase positions within the initially assumed model.

By also considering the density histogram profiles for the conventional Bas reconstruction, model-driven reconstruction, and relaxed model-driven reconstruction (figure 19(c)), it can be seen that the density spread has been successfully reduced in the relaxed model-driven reconstruction (orange) compared to the unrelaxed model-driven reconstruction (blue). Both the unrelaxed and relaxed model-driven reconstructions exhibit unimodal distributions, as opposed to the conventional Bas reconstruction (green) that has a bimodal distribution. This implies that the multiphase density distortions in the Bas reconstruction corresponding to the two majority material phases present (SiGe and SiO_2) have largely been corrected for by the model-driven protocol.

This reconstruction of the finFET device verifies that our new model-driven APT reconstruction protocol can successfully correct for multiphase distortions within non-axisymmetric general specimen structures, even in cases where trajectory distortions and local changes in magnification are relatively extreme.
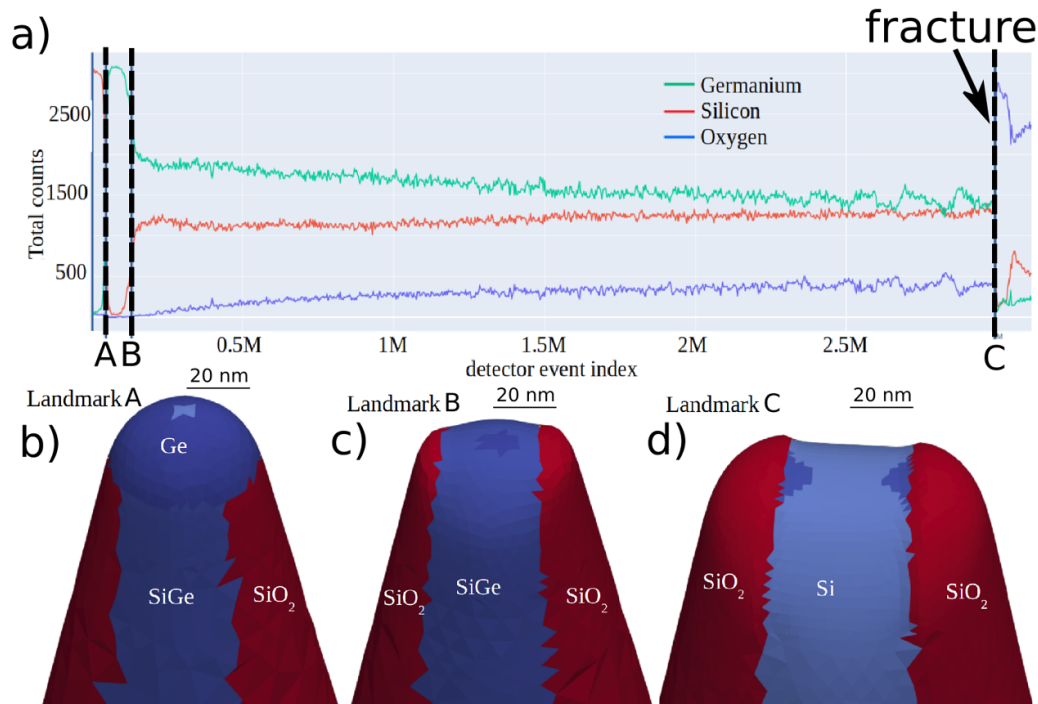
Figure 17. (a) Histograms (200 bins) for major ionic species showing landmark positions in the experimental evaporation sequence. (b)–(d) Model surface states at marked landmarks B-D. As vertical landmark positioning remained unchanged from our previous study [7]. Reproduced from [7]. © The Author(s). Published by IOP Publishing Ltd. CC BY 4.0.

5. Limitations and improvements

This study builds on our previous continuum modelling and APT image prediction from [6, 7]. By applying the results from this continuum model, a new model-driven reconstruction protocol has been demonstrated on a SiGe multilayer and finFET device experimental APT dataset, successfully correcting for multiphase distortions. Unlike previous reconstruction attempts leveraging this continuum model [7], model parameters have been automatically calibrated by optimising the similarity between the final generated reconstruction, and our prior knowledge of the specimen structure.

The numerical limitations of the current evaporation model formulation and implementation were previously outlined in [6, 7]. These included the limited accuracy of the electrostatic BEM solution close to the boundary, as well as the model's poor computational scalability at higher simulation resolutions. Such issues could potentially be resolved through higher-order collocation or Galerkin BEM approaches [43, 44], fast marching velocity extension methods, narrow band or adaptive grid level set methods [45–47], and additional BEM compression techniques [43, 48].

The current model does not fully include the instrument chamber, specimen holder, and a complete specimen shank within the electrostatic field solution. As a result, an additional image compression (section 3.2) has had to be applied to calculated ion trajectories in order to achieve an image compression comparable to that observed in experiment. It is currently unclear to the authors the exact extent to which this assumed trajectory transfer function is valid for general

heterogeneous structures. However, comparative simulations of the fields surrounding heterogeneous and homogeneous material apex shapes show that the electric fields increasingly conform with increasing distance from the surface (see section I of the supplementary material). As mathematical projection laws are known to well approximate the charged optics of homogeneous material apex shapes [4, 5], these results provide some support for the study's use of a projection-based trajectory transfer function.

It is also worth briefly commenting on the physical accuracy of the current evaporation model. Both the multilayer and finFET datasets were obtained under the APT laser-assisted evaporation mode. It is known from experiment that the presence of the laser can significantly effect the specimen apex shape, e.g. anisotropic blunting of the apex [49]. Therefore, whilst the tilting distortions in the SiGe multilayer system have been successfully reduced by the assumed model through specimen-detector spatial realignment (figure 11), the true major cause of this tilting could be from laser apex blunting. Further simulation results supporting this hypothesis can be found in section II of the supplementary material. Future work should explore validation of the model-driven approaches' compositional accuracy through correlative techniques, such as EDS.

Additionally, specimen faceting has been omitted from the specimen models during data reconstruction due to a current lack in understanding of the relevant evaporation physics at a continuum-scale. Previously, a simple non-physical model reproducing faceting was proposed in [7]. This faceting is clearly present as low density
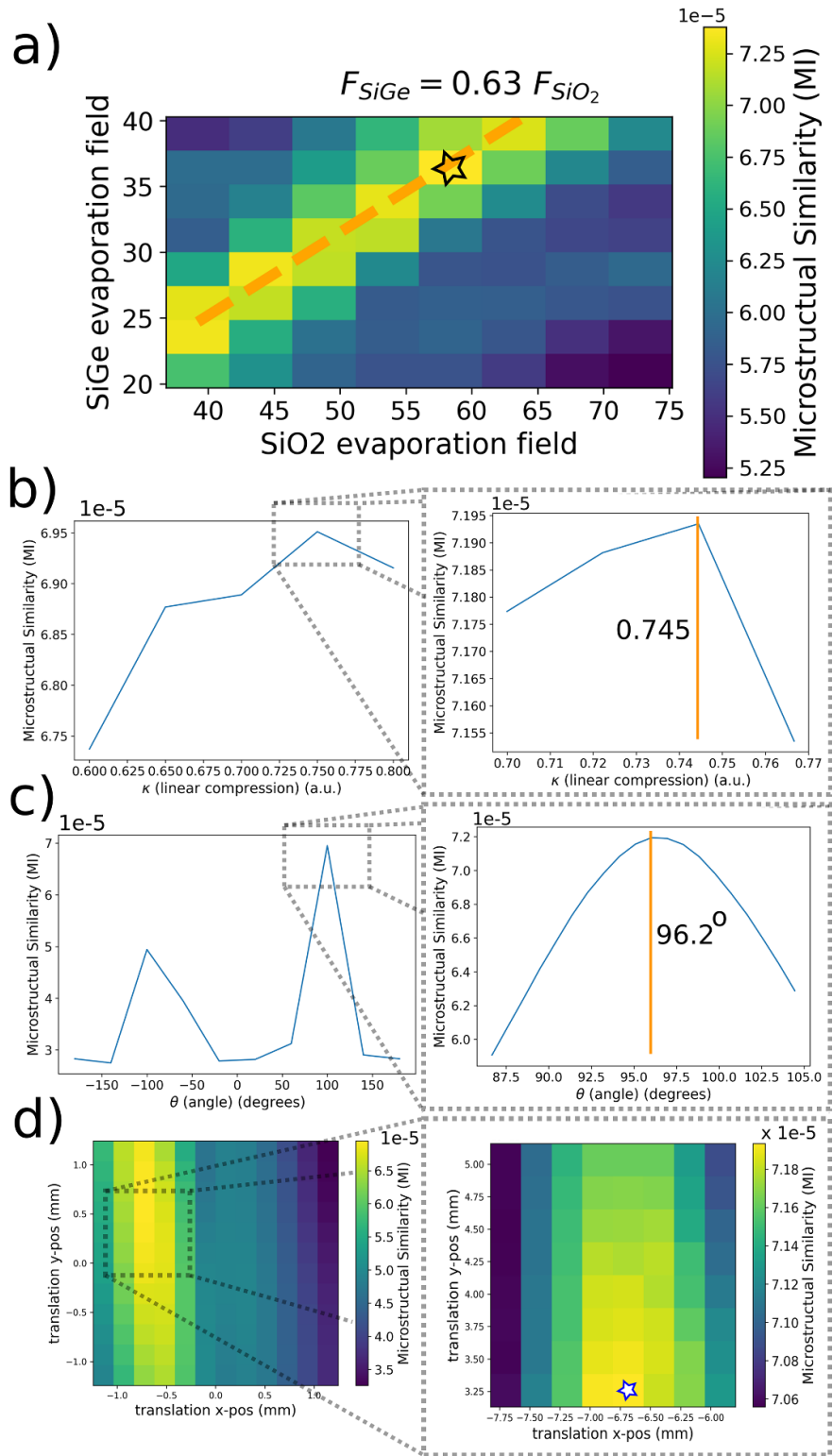
J. Phys. D: Appl. Phys. **55** (2022) 375301

C Fletcher *et al*

Figure 18. (a) Visualisation of 8×8 regular grid search over F_{SiO_2} and F_{SiGe} measuring microstructure similarity via mutual information (MI) in detector space. (b) Partial MI maximisation of the image compression (κ) through an adaptive grid search. (c) Partial MI maximisation of rotation around the analysis axis (θ) through an adaptive grid search. (d) Partial MI maximisation of the translation vector ($\vec{\mathbf{r}}$) through an adaptive grid search.

poles in the experimental datasets (see figure 12), and whilst the model relaxation step can partially correct for these pole distortions, future continuum models should

aim to physically capture this demagnification occurring at surface facets. The authors suspect that doing so will likely require a multiscale modelling approach in order to
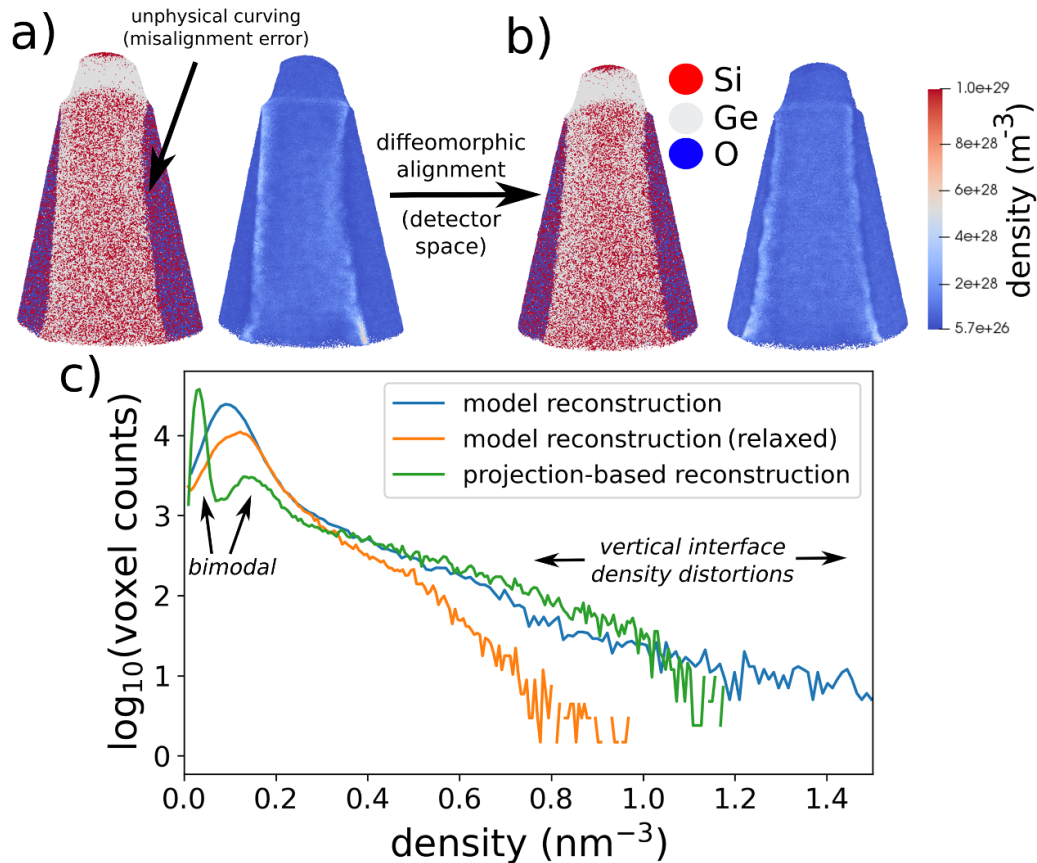
Figure 19. (a) Front-facing orientation of parameter-constrained reconstruction showing local composition and density. (b) Same orientation of reconstruction following interface alignment via the diffeomorphic density matching transformation. (c) Histogram for local voxel densities (200 bins) for the different reconstructions. It can be seen that the diffeomorphism-aligned model-driven reconstruction features a reduced density spread, particularly at the higher densities associated with vertical interfaces.

fully capture the atomic-scale evaporation ordering effects responsible [23].

The current parameter optimisation procedure is performed via either a regular grid search or adaptive grid search approach. While alternative local optimisation methods would converge in fewer model iterations [31], these could potentially miss the global maximum in similarity [12]. For larger model parameter searches, a random search might outperform this grid search approach [50]. For more complex models than those considered, running parameter optimisations on distributed computing clusters will almost certainly become essential to achieve practical computation times. Computation times could be further reduced through additional numerical improvements to the driving model. For example, the adaptive surface remeshing currently required by the driving model is preventing the model from being fully parallelisable [7]. A solution to this could be replacing the BEM with a meshfree solver [51].

Whilst successfully correcting distortions in semiconductor datasets, the protocol remains technically challenging and additional progress is required before a widely applicable model-driven reconstruction protocol is achieved. The current workflow still requires significant user input, such as the initial geometry, and some preprocessing, such as landmark placement in the detector event sequence. The potential to further

reduce user input and automate the analysis through data-driven approaches could prove critical for its wider adoption within the APT community.

Finally, it should be noted that the continuum modelling framework is largely independent from the assumed law governing material evaporation (equation (1)). Therefore, this law can be readily swapped out for alternative forms without requiring significant modifications to the model. By enabling the simulation of structures that are directly comparable to experimental data, this modelling framework could be used to explore and test new forms for evaporation laws, and aid in validating our current understanding of field evaporation theory. In turn, more accurate prediction of model evaporation and resulting specimen apex shape changes could reduce residual errors within model-driven reconstructions.

6. Conclusions

In this study, a new model-driven reconstruction protocol has been outlined, capable of correcting for multiphase distortions within experimental APT data. Unknown model parameters such as phase evaporation fields and specimen orientation have been automatically tuned by maximising the similarity between local composition in the generated reconstruction,

J. Phys. D: Appl. Phys. **55** (2022) 375301

C Fletcher *et al*

and the prior knowledge of local phase in the original specimen structure. Through this new approach, distortions within a semiconductor multilayer system and a finFET device have been significantly reduced. An additional model relaxation step, that applies a diffeomorphic density matching algorithm developed for computational anatomy, was also applied to the finFET dataset, further reducing multiphase distortions.

A new method was also outlined for efficiently predicting detector density hitmaps, as well as predicting detector regions where trajectory crossover is occurring. In the future, such an approach could allow the partial correction of composition biases arising from this spatial crossover within reconstructions.

The successful model-driven reconstruction of two differing semiconductor datasets clearly demonstrates this new protocol's superiority over conventional projection-based protocols for reducing APT image distortions in semiconductor devices: material systems critical for modern society that are widely and routinely analysed in both research and industry.

Data availability statement

The data that support the findings of this study are openly available at the following URL/DOI: https://doi.org/10.7910/DVN/FHEXDI.

Acknowledgments

Source code and experimental data

The source code for both the model and automated reconstruction protocol is available at https://gitlab.com/fletchie/casra-3d. Both the experimental finFET and SiGe multilayer datasets (both APT and electron microscopy data) can be obtained at [52]. All simulations have been performed on Ubuntu 20.04 using system Python 3.8, with Python library versions installed via apt and linked against OpenBLAS version 0.3.8. All dependency library versions used are fully specified by the Ubuntu distribution, and can be checked at https://packages.ubuntu.com/. Simulations were performed on the same desktop (Ryzen 7 CPU system with 8 real cores running at 3.4 GHz).

A new version of this code (CASRA^{++}) is also under development, with the aim to refactor the existing codebase into a more user-friendly program. The latest version of this program can be found at https://gitlab.com/fletchie/casra.

ORCID iDs

Charles Fletcher ⓘ https://orcid.org/0000-0003-2179-296X
Michael P Moody ⓘ https://orcid.org/0000-0002-9256-0966
Claudia Fleischmann ⓘ https://orcid.org/0000-0003-1531-6916
Clement Porret ⓘ https://orcid.org/0000-0002-4561-348X

References

[1] Southworth H N and Walls J M 1978 The projection geometry of the field-ion image *Surf. Sci.* **75** 129–40
[2] Blavette D, Sarrau J M, Bostel A and Gallot J 1982 Direction et distance d'analyse à la sonde atomique *Rev. Phys. Appl.* **17** 435–40
[3] Bas P, Bostel A, Deconihout B and Blavette D 1995 A general protocol for the reconstruction of 3D atom probe data *Appl. Surf. Sci.* **87–88** 298–304
[4] Cerezo A, Warren P J and Smith G D W 1999 Some aspects of image projection in the field-ion microscope *Ultramicroscopy* **79** 251–7
[5] De Geuser F and Gault B 2017 Reflections on the projection of ions in atom probe tomography *Microsc. Microanal.* **23** 238–46
[6] Fletcher C, Moody M P and Haley D 2019 Fast modelling of field evaporation in atom probe tomography using level set methods *J. Phys. D: Appl. Phys.* **52** 435305
[7] Fletcher C, Moody M P and Haley D 2020 Towards model-driven reconstruction in atom probe tomography *J. Phys. D: Appl. Phys.* **53** 475303
[8] Oberdorfer C 2014 Numeric simulation of atom probe tomography *PhD Dissertation* University of Münster
[9] Rolland N, Vurpillot F, Duguay S and Blavette D 2015 Dynamic evolution and fracture of multilayer field emitters in atom probe tomography: a new interpretation *Eur. Phys. J.: Appl. Phys.* **72** 21001
[10] Oberdorfer C, Withrow T, Yu L J, Fisher K, Marquis E A and Windl W 2018 Influence of surface relaxation on solute atoms positioning within atom probe tomography reconstructions *Mater. Charact.* **146** 324–35
[11] Mouton I, Printemps T, Grenier A, Gambacorti N, Pinna E, Tiddia M, Vacca A and Mula G 2017 Toward an accurate quantification in atom probe tomography reconstruction by correlative electron tomography approach on nanoporous materials *Ultramicroscopy* **182** 112–7
[12] Mouton I, Katnagallu S, Makineni S K, Cojocaru-Mirédin O, Schwarz T, Stephenson L T, Raabe D and Gault B 2019 Calibration of atom probe tomography reconstructions through correlation with electron micrographs *Microsc. Microanal.* **25** 301–8
[13] Miller M K and Forbes R G 2014 Field evaporation and related topics *Atom-Probe Tomography: The Local Electrode Atom Probe* (Berlin: Springer) ch 3, pp 111–87

[14] Sussman M, Smereka P and Osher S 1994 A level set approach for computing solutions to incompressible two-phase flow *J. Comput. Phys.* **114** 146–59

[15] Fletcher C 2021 Model-driven reconstruction in atom probe tomography *PhD Dissertation* University of Oxford (available at: https://ora.ox.ac.uk/objects/uuid:c37f5d70-4031-4d31-afdb-05cee63237c4)

[16] Oberdorfer C and Schmitz G 2011 On the field evaporation behavior of dielectric materials in three-dimensional atom probe: a numeric simulation *Microsc. Microanal.* **17** 15–25

[17] Haley D, Petersen T C, Ringer S P and Smith G D W 2011 Atom probe trajectory mapping using experimental tip shape measurements *J. Microsc.* **244** 170–80

[18] Felfer P and Cairney J M 2016 A computational geometry framework for the optimisation of atom probe reconstructions *Ultramicroscopy* **169** 62–68

[19] Lloyd M J, Abernethy R G, Gilbert M R, Griffiths I, Bagot P A J, Nguyen-Manh D, Moody M P and Armstrong D E J 2019 Decoration of voids with rhenium and osmium transmutation products in neutron irradiated single crystal tungsten *Scr. Mater.* **173** 96–100

[20] Wang X *et al* 2020 Interpreting nanovoids in atom probe tomography data for accurate local compositional measurements *Nat. Commun.* **11** 1022

[21] Walls J M and Southworth H N 1979 Magnification in the field-ion microscope *J. Phys. D: Appl. Phys.* **12** 657–67

[22] Miller M K and Hetherington M G 1991 Local magnification effects in the atom probe *Surf. Sci.* **246** 442–9

[23] Vurpillot F, Bostel A and Blavette D 2000 Trajectory overlaps and local magnification in three-dimensional atom probe *Appl. Phys. Lett.* **76** 3127–9

[24] Niewieczerzał D, Oleksy C and Szczepkowicz A 2010 Image deformation in field ion microscopy of faceted crystals *Ultramicroscopy* **110** 234–41

[25] Lawitzki R, Stender P and Schmitz G 2021 Compensating local magnifications in atom probe tomography for accurate analysis of nano-sized precipitates *Microsc. Microanal.* **27** 499–51

[26] Botsch M, Kobbelt L, Pauly M, Alliez P and Levy B 2010 Parameterisation *Polygon Mesh Processing* 1st edn (Natick, MA: A K Peters) pp 71–73

[27] Foley J D, van Dam A, Feiner S K and Hughes J 1995 *Computer Graphics: Principles and Practice* (Boston, MA: Addison-Wesley)

[28] Moody M P, Tang F, Gault B, Ringer S P and Cairney J M 2011 Atom probe crystallography: characterization of grain boundary orientation relationships in nanocrystalline aluminium *Ultramicroscopy* **111** 493–9

[29] Cover T M and Thomas J A 1991 Entropy, relative entropy and mutual information *Elements of Information Theory* (New York: Wiley) pp 13–56

[30] Powell M J D 1964 An efficient method for finding the minimum of a function of several variables without calculating derivatives *Comput. J.* **7** 155–62

[31] Nelder J A and Mead R 1965 A simplex method for function minimization *Comput. J.* **7** 308–13

[32] Sturges H A 1926 The choice of a class interval *J. Am. Stat. Assoc.* **21** 65–66

[33] De Geuser F, Lefebvre W, Danoix F, Vurpillot F, Forbord B and Blavette D 2007 An improved reconstruction procedure for the correction of local magnification effects in three-dimensional atom-probe *Surf. Interface Anal.* **39** 268–72

[34] Melkonyan D, Fleischmann C, Arnoldi L, Demeulemeester J, Kumar A, Bogdanowicz J, Vurpillot F and Vandervorst W 2017 Atom probe tomography analysis of SiGe fins embedded in SiO_2: facts and artefacts *Ultramicroscopy* **179** 100–7

[35] Rottman C, Bauer M, Modin K and Joshi S 2015 Weighted diffeomorphic density matching with applications to thoracic image registration *Proc. 5th MICCAI Workshop on Mathematical Foundations of Computational Anatomy (MFCA)* (arXiv:1508.02543)

[36] Bauer M, Joshi S and Modin K 2015 Diffeomorphic density matching by optimal information transport *SIAM J. Imaging Sci.* **8** 1718–51

[37] Epanechnikov V A 1969 Non-parametric estimation of a multivariate probability density *Theory Probab. Appl.* **14** 153–8

[38] Modin K 2017 *ddmatch* (available at: https://github.com/kmodin/ddmatch)

[39] Beg M F, Miller M I, Trouvé A and Younes L 2005 Computing large deformation metric mappings via geodesic flows of diffeomorphisms *Int. J. Comput. Vis.* **61** 139–57

[40] Ashburner J 2007 A fast diffeomorphic image registration algorithm *NeuroImage* **38** 95–113

[41] Gilbert P 1972 Iterative methods for the three-dimensional reconstruction of an object from projections *J. Theor. Biol.* **36** 105–17

[42] Gault B, Moody M P, Cairney J M and Ringer S P 2012 *Atom Probe Microscopy* (New York: Springer)

[43] Yijun L 2009 *Fast Multipole Boundary Element Method: Theory and Applications in Engineering* 1st edn (Cambridge: Cambridge University Press)

[44] Sutradhar A, Paulino G H and Gray L J 2008 *Symmetric Galerkin Boundary Element Method* 1st edn (Heidelberg: Springer)

[45] Chopp D L 1993 Computing minimal surfaces via level set curvature flow *J. Comput. Phys.* **106** 77–91

[46] Sussman M, Almgren A S, Bell J B, Colella P, Howell L H and Welcome M 1999 An adaptive level set approach for incompressible two-phase flows *J. Comput. Phys.* **148** 81–124

[47] Haley D, Bagot P A J and Moody M P 2018 Extending continuum models for atom probe simulation *Mater. Charact.* **146** 299–306

[48] Hackbusch W and Nowak Z P 1989 On the fast matrix multiplication in the boundary element method by panel clustering *Numer. Math.* **54** 463–91

[49] Sha G, Cerezo A and Smith G D W 2008 Field evaporation behavior during irradiation with picosecond laser pulses *Appl. Phys. Lett.* **92** 043503

[50] Bergstra J and Bengio Y 2012 Random search for hyper-parameter optimization *J. Mach. Learn. Res.* **13** 281–305

[51] Geiser B, Bunton J, Martin I, Reinhard D, Lenz D, Prosa T and Larson D 2020 A system for electrostatic reconstructions *Microsc. Microanal.* **26** 2622–3

[52] Dialameh M, Porret C, Bender H, Kundu P, Richard O, Melkonyan D, Scheerder J E, Fletcher C and Fleischmann C 2022 Correlative electron microscopy-atom probe semiconductor datasets for benchmarking atom probe reconstruction (available at: https://doi.org/10.7910/DVN/FHEXDI)